AGU PUBLICATIONS

JGR

Journal of Geophysical Research: Space Physics

RESEARCH ARTICLE
10.1002/2017JA024736

Key Points:
- Analytical modeling of steady state conditions at Jupiter's magnetopause can be used to assess the operation of fundamental processes at the boundary
- Magnetopause reconnection site locations and reconnection rates are most sensitive to changes in the interplanetary magnetic field
- The equatorial dawn flank region of the magnetopause that is Kelvin-Helmholtz unstable is less sensitive to changing conditions

Supporting Information:
- Supporting Information S1

Correspondence to:
A. Masters,
a.masters@imperial.ac.uk

Citation:
Masters, A. (2017). Model-based assessments of magnetic reconnection and Kelvin-Helmholtz instability at Jupiter's magnetopause. *Journal of Geophysical Research: Space Physics*, *122*. https://doi.org/10.1002/2017JA024736

Received 1 SEP 2017
Accepted 24 OCT 2017
Accepted article online 30 OCT 2017

Model-Based Assessments of Magnetic Reconnection and Kelvin-Helmholtz Instability at Jupiter's Magnetopause

A. Masters[1]

[1]Blackett Laboratory, Imperial College London, London, UK

Abstract The interaction between the solar wind and Jupiter's magnetic field confines the planetary field to the largest magnetosphere in the Solar System. However, the full picture of when and where key processes operate at the magnetopause boundary of the system remains unclear. This is essential for testing understanding with observations and for determining the relative importance of different drivers of Jovian magnetospheric dynamics. Here we present a global analytical model of Jovian magnetopause conditions under steady state, which forms the basis of boundary process assessments. Sites of magnetic reconnection at Jupiter's magnetopause are expected to be in regions of sufficiently high magnetic shear across the boundary, controlled by the orientation of the interplanetary magnetic field. Reconnection rates are also most sensitive to changes in the highly variable IMF, followed by changes in the solar wind plasma mass density. The largest plasma flow shear across the boundary is in the equatorial dawn region, producing a region that is typically unstable to growth of the Kelvin-Helmholtz (K-H) instability. Compared to magnetopause reconnection site locations, this K-H-unstable region at dawn is less sensitive to changing conditions. Motion of K-H boundary perturbations typically includes dawn-to-dusk motion across the subsolar region. Model-predicted reconnection voltages are typically hundreds of kV but rely on steady solar wind conditions on a time scale that is longer than typical at Jupiter's orbit. How the reconnection voltage compares to the voltage applied due to the "viscous-like" interaction involving K-H instability remains unclear.

1. Introduction

The interaction between the supersonic flow of collisionless solar wind plasma and a strongly magnetized planet leads to the effective confinement of the planetary magnetic field to a cavity within the flow, known as a planetary magnetosphere. Jupiter has the largest magnetosphere in the Solar System, due to a combination of prevailing solar wind conditions, a strong planetary magnetic field, and appreciable magnetospheric plasma populations (see the reviews by Dessler, 1983, and in Bagenal et al., 2004). The Jupiter system is presently the subject of in situ exploration by the *Juno* spacecraft (e.g., Bagenal et al., 2014) and remote observation from Earth and space-based platforms (e.g., the *Hubble Space Telescope*, *Hisaki* spacecraft). One of the major open issues currently being addressed by the scientific community is the question of exactly how the solar wind affects the giant Jovian magnetosphere and what are the implications of this external influence on the system.

Near-Jupiter solar wind measurements made by a range of spacecraft have constrained the typical state of the magnetized solar wind plasma at this heliocentric distance but have also shown that most solar wind properties are highly dynamic (Ebert et al., 2014; Gruesbeck et al., 2017; Jackman & Arridge, 2011). Since the location of the magnetopause boundary of the magnetosphere is controlled by total pressure balance, the frequent, and often dramatic changes in solar wind dynamic pressure lead to expansion and contraction of the Jovian magnetospheric cavity, which represents one of the most obvious solar wind influences on the system (Ebert et al., 2010; Gershman et al., 2017; Huddleston et al., 1998; Joy et al., 2002; Kurth et al., 2002).

Evidence of solar wind control of Jovian auroral emissions has been widely reported and generally indicates a positive correlation between the solar wind dynamic pressure and auroral power (Badman et al., 2016; Baron et al., 1996; Barrow, 1978, 1979; Barrow et al., 1986; Clarke et al., 2009; Dunn et al., 2016; Echer et al., 2010; Galopeau & Boudjada, 2005; Genova et al., 1987; Grodent et al., 2003; Gurnett et al., 2002; Hess et al., 2014, 2012; Kaiser, 1993; Kimura et al., 2016; Kita et al., 2016; Ladreiter & Leblanc, 1989; Nichols et al., 2007, 2017; Prangé et al., 2001, 2004; Pryor et al., 2005; Terasawa et al., 1978; Waite et al., 2001; Zarka & Genova, 1983);

however, rapid compression of the magnetosphere does not necessarily produce a clear auroral response, and some auroral intensifications appear to be unassociated with solar wind variability (Clarke et al., 2009; Kimura et al., 2015). The magnetospheric dynamics underlying the response of the Jovian aurora to the solar wind has been widely discussed (Chané et al., 2017; Cowley & Bunce, 2001, 2003; Delamere & Bagenal, 2010, 2013; Southwood & Kivelson, 2001; Walker et al., 2001).

In addition to causing dramatic changes in the size of Jupiter's magnetosphere the solar wind conditions also control the operation of processes at the magnetopause that lead to energy transfer across the boundary. Magnetic reconnection is one such process, which changes the local structure of the magnetic field and converts magnetic energy into particle kinetic energy (Dungey, 1961) (see the reviews by Vasyliunas, 1975, and Paschmann et al., 2013). Reported analyses of in situ spacecraft observations at Jupiter's magnetopause have provided evidence for reconnection, in the form of the magnetic signatures expected to result from reconnection (Gershman et al., 2017; Huddleston et al., 1997), identified encounters with examples of the reconnection-related phenomenon of flux transfer events (Huddleston et al., 1997; Walker & Russell, 1985), and the most compelling evidence in the form of direct detection of reconnection outflow (Ebert et al., 2017). Another key process expected to operate at Jupiter's magnetopause is growth of the Kelvin-Helmholtz (K-H) instability, where bulk flow shears across the boundary can lead to the growth and motion of boundary perturbations, forming waves and subsequently vortices (e.g., Hasegawa et al., 2004; Miura & Pritchett, 1982).

The expected operation of these two processes at Jupiter's magnetopause was explored by Desroche et al. (2012), who combined simple mathematical descriptions of steady state near-magnetopause conditions to consider the global magnetopause surface of the dayside and near-magnetotail. These authors considered a limited range of potential external (solar wind) and internal (magnetospheric) conditions at the boundary and showed the expected impact of Jupiter's polar-flattened magnetopause on the draping of the interplanetary magnetic field (IMF) around the surface (Erkaev et al., 1996; Farrugia et al., 1998). In addition, Desroche et al. (2012) highlight the potential negative impact of large cross-magnetopause flow shears and pressure gradients on reconnection at the boundary, and their results support the expected dawn-dusk asymmetry in magnetopause K-H stability resulting from the prevailing magnetospheric flow.

The present study builds on the work of Desroche et al. (2012) by continuing to use a simple analytical modeling approach to assess the operation of Jovian magnetopause processes. We extend the scope of these assessments and consider a wider range of conditions at the boundary, also under steady state. In the following sections we describe the foundations of the modeling approach in studies of the terrestrial magnetopause, and its recent application to Saturn, Uranus, and Neptune. We then use the Jupiter model to consider a range of conditions at the Jovian magnetopause, assessing the expected operation of magnetic reconnection and growth of the K-H instability. The context and hypotheses provided by this modeling are essential for testing our understanding of these fundamental plasma processes in the Jovian magnetopause environment and subsequently for answering the question of how the solar wind influences Jupiter's magnetosphere.

2. Modeling Conditions at Jupiter's Magnetopause Under Steady State

Combining simple mathematical expressions to approximate the global picture of conditions adjacent to a planetary magnetopause has been extensively used to investigate the interaction between the solar wind and Earth's magnetosphere (Cooling et al., 2001; Crooker, 1979; Dunlop et al., 2011; Fuselier et al., 2016, 2011, 2017; Gomez et al., 2016; Kobel & Flückiger, 1994; Komar et al., 2015; Luhmann et al., 1984; Petrinec & Russell, 1997; Petrinec et al., 2016, 2011, 2003, 2014; Souza et al., 2017; Trattner et al., 2016, 2007a, 2007b, 2015, 2012, 2017; Vines et al., 2017; Wilder et al., 2014). This considerable terrestrial modeling heritage formed the foundation of recent, similar investigations of the solar wind interaction with Saturn, Uranus, and Neptune (Masters, 2014, 2015a, 2015b), and these giant planet models are precursors of the present Jupiter model. In this section we describe exactly how this modeling approach is applied to Jupiter.

An overview of the steps involved in the modeling is shown in Figure 1. There are 11 inputs to the model (upper text boxes in Figure 1), which define a model magnetopause surface mesh, and ultimately lead to magnetized plasma conditions adjacent to all points on the surface under steady state. The specified IMF is constrained to be perpendicular to the solar wind flow (see section 3). These conditions then lead to the

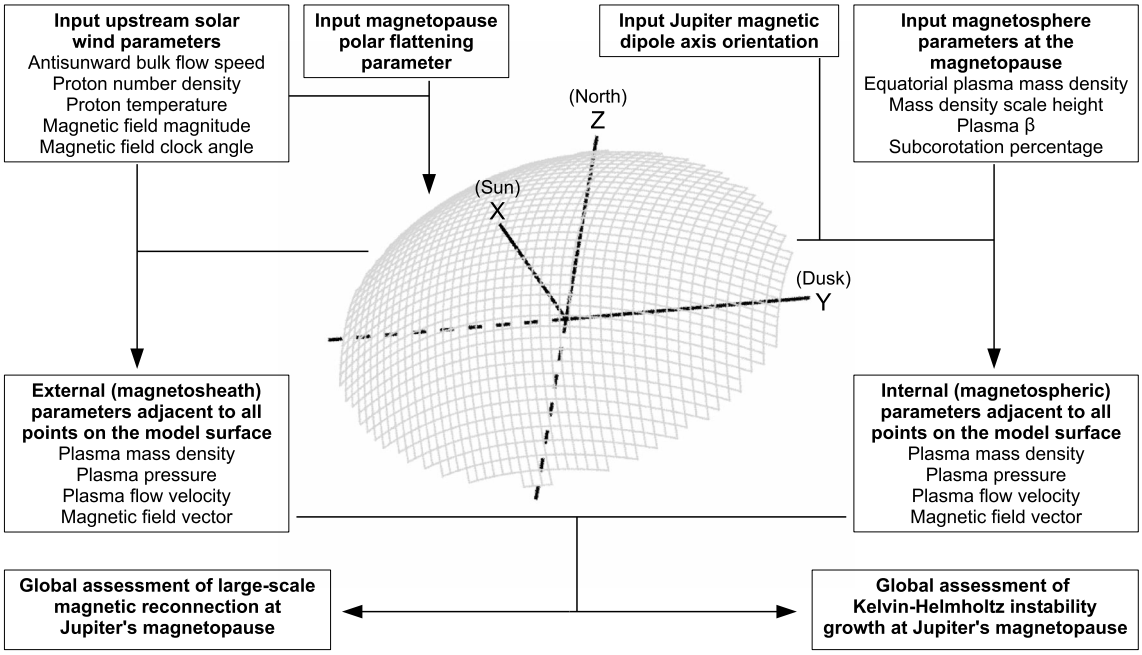

Figure 1. Illustration of approach to modeling conditions at Jupiter's magnetopause under steady state.

model outputs, a global assessment of both magnetopause reconnection and growth of the K-H instability. The coordinate system used throughout this paper has its origin at the center of Jupiter, with the *x* axis pointing toward the Sun, the *y* axis defining an *xy* plane that contains Jupiter's orbital velocity vector (with a negative projection of the *y* axis on this vector), and the *z* axis completing the orthogonal right-handed set (pointing north out of the ecliptic). The solar wind upstream of Jupiter's bow shock is referred to as the "upstream solar wind," whereas the shocked solar wind downstream of the bow shock that flows around the magnetosphere is referred to as the "magnetosheath." Note that the IMF is the upstream solar wind magnetic field.

The first step in the modeling is the definition of the magnetopause surface itself. We take the dynamic pressure corresponding to the input upstream solar wind conditions, where we assume a charge-neutral plasma with an ion composition of 96% protons and 4% doubly ionized Helium by number. We then calculate the distance between the origin and both the bow shock and magnetopause along the *x* axis (the bow shock and magnetopause standoff distances) using the power law relationships with solar wind dynamic pressure presented by Joy et al. (2002). The functional form used to describe the full magnetopause surface is a parabolic conic section with its focus at the origin, which is then flattened in the *z* direction. The *x* coordinate of a point on the surface is given as

$$x = R - \left(\frac{y^2 + (Fz)^2}{4R}\right) \tag{1}$$

where R is the magnetopause standoff distance and F is a flattening parameter. The case of F equal to 1 corresponds to a parabolic conic section that is axissymmetric about the *x* axis. Increasing the F value from 1 leads to increasing flattening of the surface in the *z* direction. Inclusion of this flattening parameter allows the model to approximate the magnetopause shape that results from the largely equatorial confinement of magnetospheric plasma mass that results from centrifugal forces (see below discussion of magnetospheric conditions) (e.g., Desroche et al., 2012; Joy et al., 2002). In this study we limit our consideration of the Jovian magnetopause to the dayside ($x > 0$).

The calculation of magnetosheath plasma parameters immediately external to every point on the model magnetopause surface is based on the equations presented in Masters (2014), which are taken from Petrinec and Russell (1997). These authors derived expressions for plasma flow speed, mass density, and pressure at the boundary of an obstacle under steady state for the case of hydrodynamic flow (i.e., in

the absence of a magnetic field). These expressions are functions of upstream solar wind parameters and the local orientation of the magnetopause surface only. Note that in order to calculate the upstream solar wind plasma pressure we assume the relationship between solar wind proton and electron temperatures given by Slavin and Holzer (1981). The magnetosheath flow speed and direction is later modified, as described below, but is initially set to be directed away from the subsolar point (the point on the surface with a y coordinate and z coordinate equal to 0) and tangential to the local magnetopause surface everywhere.

As discussed by Petrinec and Russell (1997), the inclusion of an IMF in this analytical treatment and subsequent derivation of expressions for magnetosheath magnetic field (draped IMF) and plasma parameters at the magnetopause is only possible for the case of an IMF that is parallel or antiparallel to the upstream solar wind velocity. In the majority of similar previous modeling studies cited at the beginning of this section the draped IMF immediately adjacent to the magnetopause was calculated using the expressions derived by Kobel and Flückiger (1994), who considered a current-free magnetosheath region bounded by an axissymmetric paraboloid bow shock and magnetopause. However, the flattening of our model Jovian magnetopause surface affects the magnetosheath magnetic field structure due to preferential flow over the poles that leads to twisting of magnetosheath field lines toward the z direction (Desroche et al., 2012; Erkaev et al., 1996; Farrugia et al., 1998). For application to Jupiter we therefore modify the approach taken in relevant previous work (e.g., Masters, 2014).

We refer the reader to the supporting information for an annotated example of our magnetosheath field modeling approach. We first project the specified IMF on to the magnetopause subsolar point and assume this to be the local magnetosheath field direction. The stagnation magnetic field line draped around the dayside magnetopause is then determined from this starting point as the field line that is parallel or antiparallel to the modeled magnetosheath plasma flow at all points. Two further magnetosheath field lines are then defined, each of which is the stagnation field line shifted in a direction that is perpendicular to both the subsolar field direction and the subsolar magnetopause surface normal, and each by a distance equal to the shortest distance between adjacent points on the model surface. These two field lines are then advected through the magnetosheath flow pattern to give the magnetosheath field adjacent to all points on the model magnetopause surface under steady state.

To calculate the magnitude of the magnetosheath magnetic field at all points, we first build a dummy magnetopause surface that is not flattened but which is otherwise identical to our surface of interest. We then apply the classic Kobel and Flückiger (1994) draped IMF description to the dummy surface and assume an axissymmetric magnetosheath flow pattern away from the subsolar point, leading to a reference for the magnetosheath magnetic field strength as a function of the flow components parallel and perpendicular to the field direction. We use this reference to give the field strength adjacent to all points on the true model surface, by enforcing the same dependence of field strength on local flow components. The annotated example given in the supporting information attached to this paper shows the expected impact of magnetopause polar flattening on the magnetosheath field.

The final stage of the treatment of near-magnetopause magnetosheath conditions involves the modification of the flow to account for the influence of the draped magnetic field, as described by Petrinec et al. (1997) and as applied in the precursor giant planet models (e.g., Masters, 2014). While not rigorous, this modification partially addresses the limited coupling between magnetosheath plasma and magnetic field in our approach. Note that the influence of the magnetosheath Plasma Depletion Layer (PDL) as outlined in Masters (2014) is not included in the present Jupiter model (see discussion in Masters, 2015b, and section 3).

The model treatment of steady state magnetospheric parameters immediately inside the magnetopause is similar to that employed in Saturn modeling by Masters (2015b) and in past Jupiter modeling by Desroche et al. (2012). To approximate the corotation of magnetospheric plasma with the planet, the plasma flow at all points on the model magnetopause surface is perpendicular to both the planetary rotation axis (the z axis) and the local surface normal, with a speed equal to the specified (input) fraction of the local speed of rigid corotation. The distribution of magnetospheric plasma mass density at the boundary is described as an exponential decrease with absolute z coordinate, given as

$$\rho = \rho_0 e^{-\left(\frac{z}{H}\right)^2} \tag{2}$$

Table 1
Model Input Parameters Chosen to Produce Typical Conditions at Jupiter's Magnetopause Under Steady State

Parameter	Values
Upstream solar wind parameters	
Antisunward bulk flow speed[a]	400 km s^{-1}
Proton number density[a]	0.3 cm^{-3}
Proton temperature[a]	3 eV
Magnetic field magnitude[a,b,c]	1 nT
Magnetic field clock angle[a,b,c]	90° (270°)
Magnetospheric parameters at the magnetopause	
Equatorial plasma mass density[d,e,f]	5×10^{-22} kg m^{-3}
Mass density scale height[d,e,f]	10 R_J
Plasma β[f]	5
Subcorotation percentage[g]	20%
Magnetopause polar flattening parameter[h]	1.25
Jupiter Magnetic Diople Axis Orientation	*z* axis

[a]Ebert et al. (2014). [b]Jackman and Arridge (2011). [c]Gruesbeck et al. (2017). [d]Frank et al. (2002). [e]Bagenal and Delamere (2011). [f]Desroche et al. (2012). [g]Krupp et al. (2001). [h]Joy et al. (2002).

where ρ is the local mass density, ρ_0 is the specified mass density at all points where the *xy* plane intersects the model magnetopause surface, *z* is the absolute *z* coordinate, and *H* is the specified scale height. This magnetospheric plasma mass distribution is chosen to approximate the equatorial confinement of magnetospheric plasma mass that results from centrifugal forces (e.g., Desroche et al., 2012; Joy et al., 2002).

The specified ratio of plasma to magnetic pressure (plasma β) in the magnetosphere is set to be the same adjacent to all points on the model magnetopause surface. This addresses the nonnegligible plasma pressure contribution of energetic particles that are less subject to equatorial confinement but which make a negligible contribution to the local mass density. The direction of the magnetospheric magnetic field is based on a dipolar planetary magnetic field, with a dipole axis oriented as specified. The direction of the pristine planetary magnetic field at all points on the magnetopause is determined, before all vectors are rotated to be perpendicular to the local magnetopause normal, while maintaining the same direction of projection on to the surface. This results in regions of divergent and convergent magnetospheric field that represent the cusps. Finally, combining the magnetospheric plasma β requirement with the requirement of total pressure balance across the magnetopause defines the local strength of the magnetospheric magnetic field, and the local magnetospheric plasma pressure. We refer the reader to the supporting information for an assessment of how the modeled magnetospheric field at the magnetopause deviates from magnetic meridian planes (e.g., Khurana, 2001).

3. Typical Conditions at Jupiter's Magnetopause Under Steady State

In this section we define the model input values that we propose are typical and present the corresponding typical conditions at the Jovian magnetopause under steady state that result from application of the model. We then compare these conditions with published spacecraft observations.

The typical value of each model input is given in Table 1. Upstream solar wind inputs are based on published statistics of near-Jupiter solar wind measurements (Ebert et al., 2014; Gruesbeck et al., 2017; Jackman & Arridge, 2011) and the application of solar wind scaling laws to typical near-Earth conditions (Slavin & Holzer, 1981). There are two prevailing IMF directions at Jupiter, depending on whether the heliospheric current sheet is above or below the planet, and these directions are effectively parallel and antiparallel to the *y* axis (e.g., Jackman & Arridge, 2011). The IMF clock angle given in Table 1 is defined using the projection of the magnetic field vector on to the *yz* plane. A purely *z* axis projection corresponds to 0° clock angle, and the angle increases in a right-handed sense about the negative *x* axis. Clock angles of 90° and 270° therefore represent the prevailing solar wind magnetic field directions at Jupiter. We choose 90° as the typical clock angle and comment on differences with the case of 270° clock angle below. Note that we only consider upstream solar wind magnetic field vectors that lie in the *yz* plane, since this contains the prevailing directions and is more appropriate for our magnetosheath field modeling approach (see discussion in Petrinec et al., 2003). The combination of the typical upstream solar wind conditions in Table 1 gives a fast magnetosonic Mach number of 8, an Alfvén Mach number of 14, a plasma β of 2.5, and a dynamic pressure of 0.09 nPa, which leads to a magnetopause standoff distance of 75 Jovian radii (R_J; 1 R_J = 71,492 km).

The extent of magnetopause polar flattening and the typical conditions in the magnetosphere adjacent to Jupiter's magnetopause are less well constrained by observations and simulations. We set a moderately flattened magnetopause surface as typical (e.g., Joy et al., 2002) and base our choice of typical magnetospheric inputs on Desroche et al. (2012) (see also Bagenal et al., 2016). We set the typical equatorial plasma mass density in the magnetosphere and the mass density scale height to be consistent with the extension of their plasma sheet extension to the magnetopause, where their description is based on the work of Frank et al., (2002) and Bagenal and Delamere (2011). We choose a magnetospheric plasma β of 5, although this is

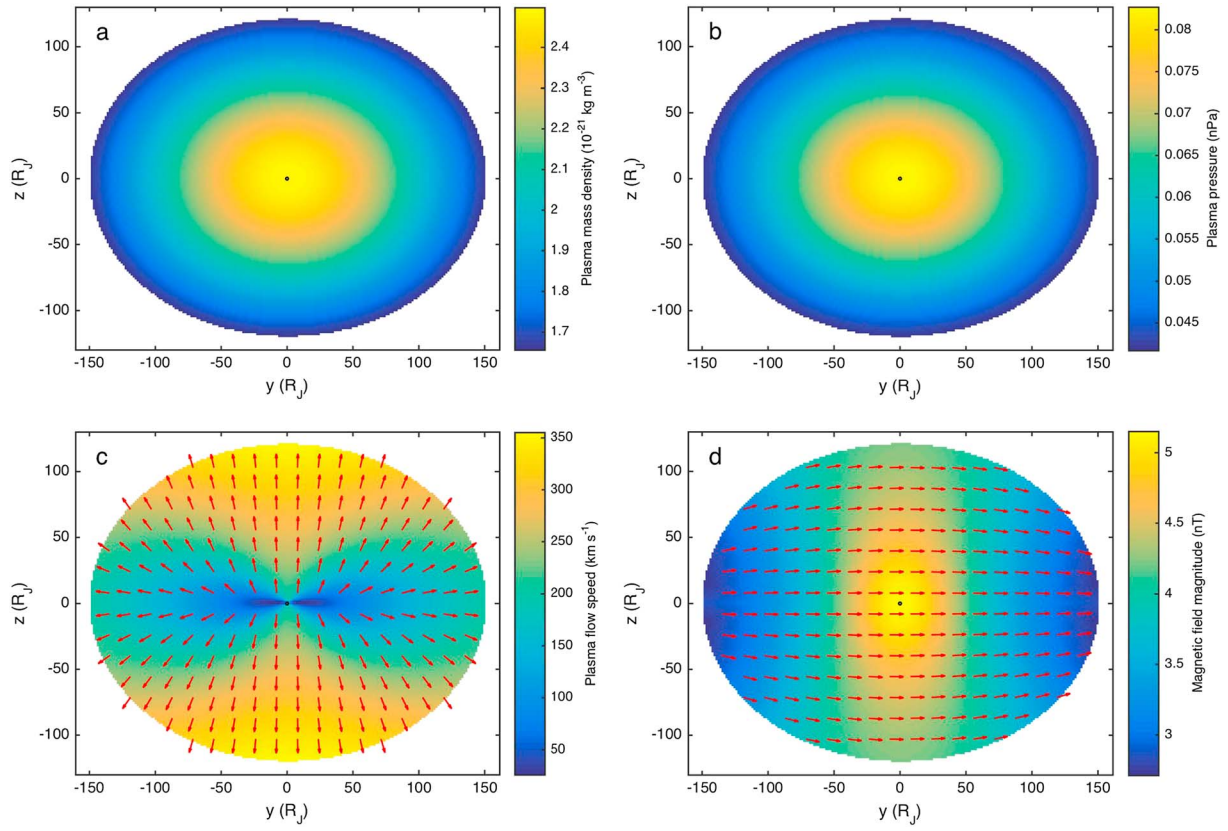

Figure 2. Typical magnetosheath solar wind conditions adjacent to Jupiter's magnetopause under steady state given by the model. In all panels the dayside model magnetopause surface is shown ($x > 0$) as viewed from the $-x$ direction (i.e., from the Sun; i.e., along the solar wind velocity vector), and Jupiter is given as a black circle at the origin. (a) Plasma mass density. (b) Plasma pressure. (c) Plasma flow speed, with flow direction indicated by arrows. (d) Magnetic field magnitude, with field direction indicated by arrows.

particularly poorly constrained (see discussion in Desroche et al., 2012). Our choice of subcorotation percentage stems from flow measurements made by the energetic particle detector on the *Galileo* spacecraft (Krupp et al., 2001). Finally, we set the orientation of Jupiter's magnetic dipole axis as parallel to the z axis (assumed to be the rotation axis due to Jupiter's low obliquity), to represent an average dipole orientation over multiple planetary rotations.

Using the values in Table 1 as model inputs produces output conditions at Jupiter's magnetopause that are presented in Figures 2 and 3. The magnetosheath solar wind conditions immediately outside the model magnetopause surface are shown in Figure 2. The plasma mass density and pressure (Figures 2a and 2b) are highest close to the subsolar point (the subsolar region), due to the pileup of plasma at the nose of the magnetospheric obstacle to the solar wind flow. The magnetosheath flow speed (Figure 2c) generally increases with distance from the subsolar point and is preferentially directed over the poles due to flattening. The influence of the magnetosheath magnetic field (Figure 2d) is to accelerate the plasma flow in the direction of the poles (perpendicular to the draped IMF direction) (Petrinec et al., 1997), which further breaks the axissymmetry of magnetosheath flow about the x axis.

The magnetospheric conditions immediately inside the model magnetopause surface are shown in Figure 3. The distribution of magnetospheric plasma mass density (Figure 3a) shows our simple approximation of equatorial confinement. Magnetospheric plasma pressure is more uniform, although it is higher in the subsolar region due to the requirement of total pressure balance across the boundary. The magnetospheric flow (Figure 3c) is dawn-to-dusk, and higher on the equatorial flanks where the local speed of rigid corotation is higher. The magnetospheric magnetic field (Figure 3d) shows simple northern and southern cusp features of divergent and convergent field and is directed southward in the equatorial region. The magnetospheric field strength is higher in the subsolar region, also due to the total pressure balance requirement.

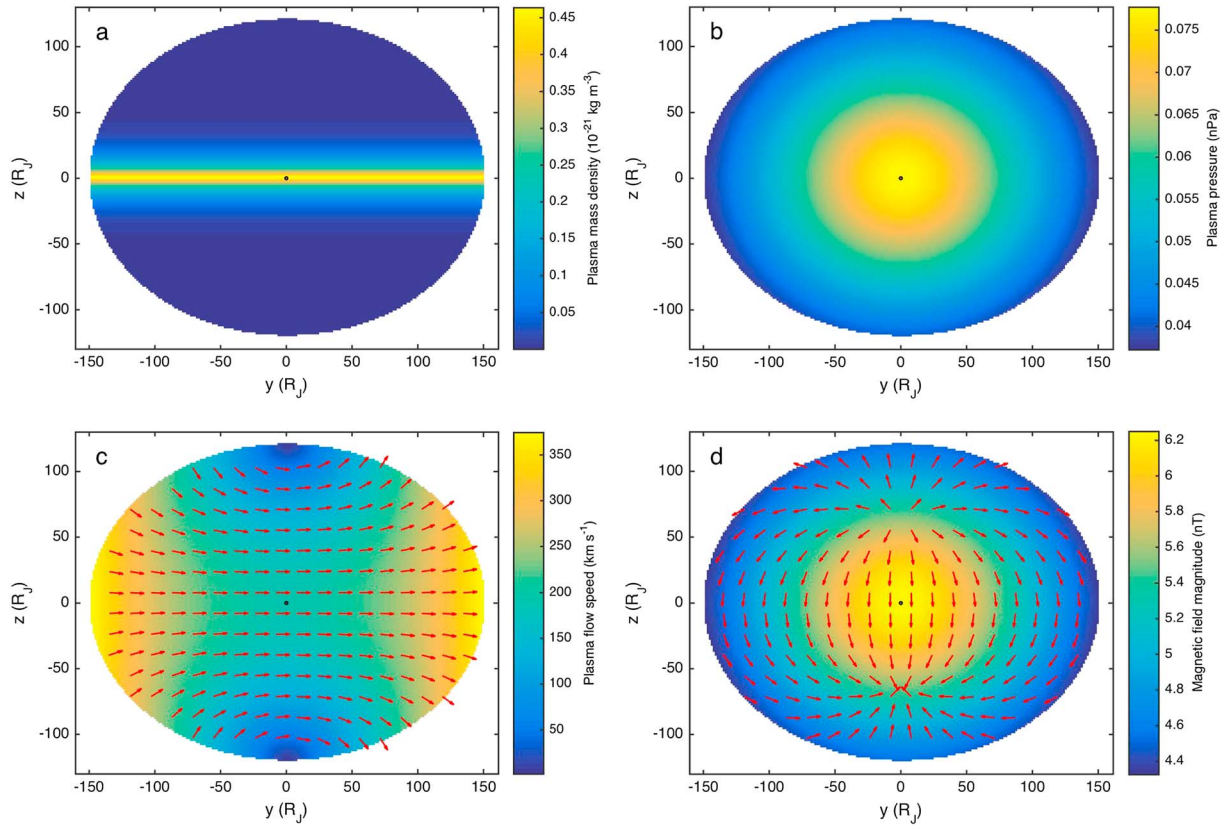

Figure 3. Typical magnetospheric conditions adjacent to Jupiter's magnetopause under steady state given by the model. In all panels the dayside model magnetopause surface is shown ($x > 0$) as viewed from the $-x$ direction (i.e., from the Sun; i.e., along the solar wind velocity vector), and Jupiter is given as a black circle at the origin. (a) Plasma mass density. (b) Plasma pressure. (c) Plasma flow speed, with flow direction indicated by arrows. (d) Magnetic field magnitude, with field direction indicated by arrows.

Published in situ measurements made by spacecraft at the Jovian magnetopause have shown that conditions are highly variable (i.e., generally not steady state, see discussion in section 4) but can be compared to these model outputs for steady, typical conditions. Dayside magnetosheath observations made by both *Voyager 1* and *Voyager 2* suggest generally low ($<$100 km s^{-1}) flow speeds and proton number densities ranging between ~1 and ~3 cm^{-3} (plasma mass densities between ~2×10^{-21} and ~5×10^{-21} kg m^{-3}) near the magnetopause in the subsolar region (Richardson, 1987), which we suggest is in broad agreement with the modeling results shown in Figures 2a and 2c. More recent observations by the *Juno* spacecraft at the equatorial dusk magnetopause effectively between a model x coordinate of 5 and -20 R_J suggest local magnetosheath plasma flow speeds of ~250 km s^{-1} directed tailward (Ebert et al., 2017; McComas et al., 2017), which is also in broad agreement with the modeling results shown in Figure 2c. Flow measurements made by *Juno* immediately inside the magnetosphere in this region suggest tailward plasma motion, in contrast to the model results shown in Figure 3c. However, the model does not consider the nightside magnetopause, and this difference may also be due to the presence of a boundary layer (see discussion in section 4).

Reported measurements of the near-magnetopause magnetic field span a range of locations and have been made by multiple spacecraft. The magnetosheath field strength just outside the dayside boundary has been measured between ~1.5 and ~10 nT (Ebert et al., 2017; Gershman et al., 2017; Hospodarsky et al., 2017; Huddleston et al., 1997; Walker & Russell, 1985). We suggest that the middle of this range is captured by the modeling results presented in this section, where the subsolar magnetosheath field strength is ~5 nT (Figure 2d). The measured magnetospheric field strength just outside the boundary is typically stronger and lies in the range ~3 to ~12 nT (Ebert et al., 2017; Gershman et al., 2017; Hospodarsky et al., 2017; Huddleston et al., 1997; Walker & Russell, 1985). We also propose that this is well captured by the modeling results, where the subsolar magnetospheric field strength is ~6 nT (Figure 3d).

Further tests of the model output conditions at Jupiter's magnetopause with future spacecraft observations are necessary. As stated in section 2, the present Jupiter modeling does not include treatment of a magnetosheath PDL (e.g., Zwan & Wolf, 1976). Inclusion of a magnetosheath PDL as described by Masters (2014) leads to modeled magnetosheath magnetic field strengths that are higher than the upper limit of the above range defined by spacecraft observations. This is consistent with Saturn modeling carried out by Masters (2015b) who also found that the exclusion of a magnetosheath PDL led to best agreement with in situ observations, likely due to overestimation of the magnetosheath field strength (prior to PDL inclusion) by the Kobel and Flückiger (1994) framework.

We suggest that the near-magnetopause conditions presented here are a good approximation of the typical environment under steady state, and these modeled conditions form the basis of our global assessments of magnetic reconnection and K-H instability at the Jovian magnetopause that are presented in the following section. However, in section 4 we place particular emphasis on the sensitivity of the assessments to using different values of each model input parameter, and the likely impact of making these inputs a function of time (i.e., no longer steady state). We propose that the conclusions we draw are robust, since they follow consideration of the underlying model assumptions and the limits of its applicability.

4. Assessing the Operation of Key Processes at Jupiter's Magnetopause

The conditions at Jupiter's magnetopause predicted by the present modeling should be regarded as highly idealized global characterizations of the adjacent environments under steady state, and in the absence of the operation of the key boundary processes that are the focus of this study. In other words, the modeling gives an overview of near-magnetopause parameters if the operation of these processes were to be "switched off." In the following subsections we separately assess the operation of two key processes using this foundation, both of which are capable of producing energy and mass transport across the Jovian magnetopause.

4.1. Large-Scale Magnetic Reconnection

We define "large-scale" magnetic reconnection at Jupiter's magnetopause as reconnection that occurs at loci of points on the magnetopause that describe "X lines" on the surface that are on a global (dayside magnetopause) scale. This is distinct from more localized and potentially intermittent reconnection (see section 4.2).

Current understanding of magnetic reconnection onset suggests that a number of conditions need to be simultaneously satisfied at a given location on a current sheet. The first of these is that the local thickness of the current sheet must be of order one ion inertial length or thinner (e.g., Phan et al., 2011; Sanny et al., 1994). The second is that the relative diamagnetic drift between ions and electrons within the current sheet must have a component in the direction of reconnection outflow that is lower than the outflow speed itself (Phan et al., 2010, 2013; Swisdak et al., 2003, 2010; Trenchi et al., 2015). The third is that the bulk flow shear in the direction of reconnection outflow must be below an upper limit that is also related to the speed of the outflow (Cassak & Otto, 2011; Doss et al., 2015).

In the present Jupiter modeling we assume that the current sheet thickness condition is satisfied at all points on the modeled dayside Jovian magnetopause, based on the report by Phan et al. (2013) who drew this conclusion concerning the terrestrial magnetopause current sheet. The onset requirement related to diamagnetic particle drifts can be applied by evaluating whether the condition

$$\theta > 2\arctan\left(\frac{d_i \Delta\beta}{2L}\right) \tag{3}$$

is satisfied at each point on the model magnetopause surface (Phan et al., 2010, 2013; Swisdak et al., 2003, 2010), where θ is the angle between the adjacent magnetic fields (the magnetic shear), d_i is an ion inertial length, $\Delta\beta$ is the absolute difference in plasma β across the current sheet, and L is the current sheet thickness (set to 1 d_i since we assume a sufficiently thin current sheet).

To apply the bulk flow shear onset condition, we also consider each point on the surface, determining the vector that is parallel/antiparallel to the reconnection outflows (if onset were to occur) as the cross product of the vector that bisects the smallest angle between the adjacent magnetic fields and the local surface normal (Swisdak & Drake, 2007). The components of the adjacent magnetic fields and flow vectors in this outflow direction are then determined to give the (potential) absolute reconnecting magnetic field components, B_1

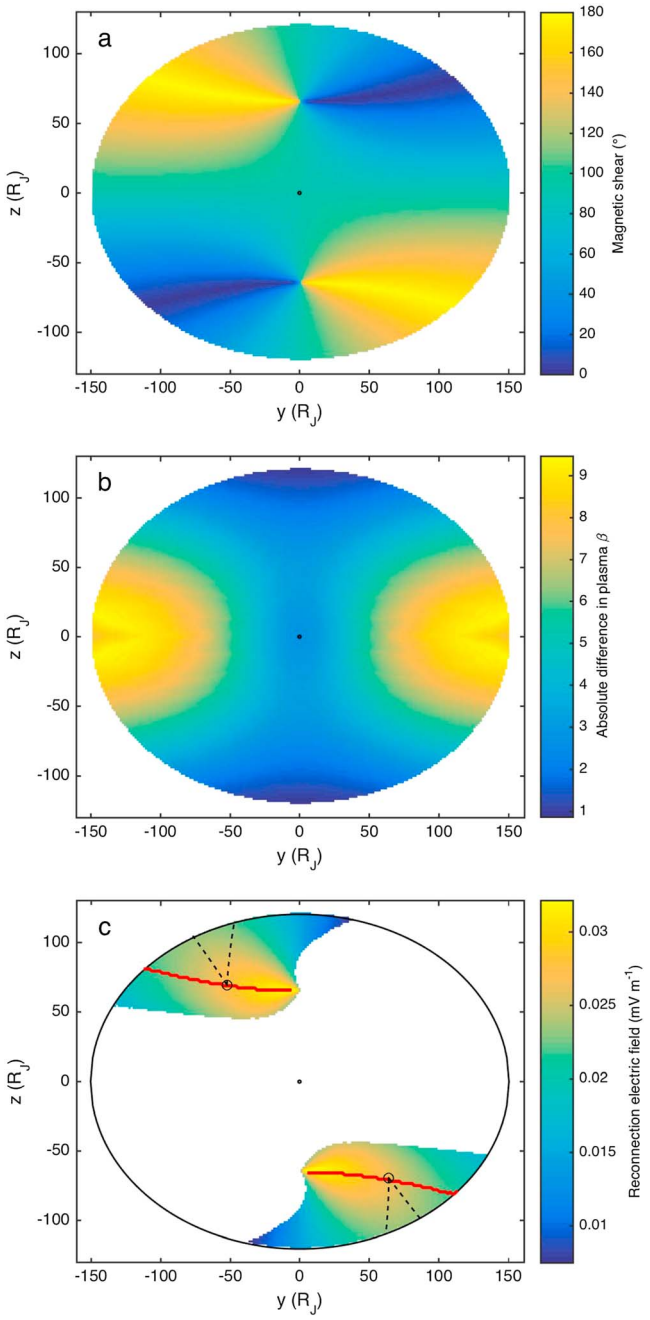

Figure 4. Assessment of large-scale magnetic reconnection at Jupiter's magnetopause under steady, typical conditions. In all panels the dayside model magnetopause surface is shown ($x > 0$) as viewed from the $-x$ direction (i.e., from the Sun; i.e., along the solar wind velocity vector), and Jupiter is given as a black circle at the origin. (a) Angle between adjacent magnetic fields (magnetic shear). (b) Absolute difference in plasma β across the boundary. (c) Reconnection electric field strength, if reconnection were to occur locally. Color only applied to regions where reconnection onset conditions are satisfied. Solid red lines give the expected location of reconnection sites as the locus of points where the magnetic shear is 180°, assumed to be the reconnection X lines. Black circles give example locations on the X lines, and dashed lines approximate the paths taken by parcels of plasma in the resulting reconnection outflow.

and B_2, and the bulk flow components, v_1 and v_2, where the subscripts 1 and 2 represent the magnetosheath and magnetospheric parameters, respectively. We then calculate the asymmetric reconnection outflow speed as

$$v_O = \left(\frac{B_1 B_2 (B_1 + B_2)}{\mu_0(\rho_1 B_2 + \rho_2 B_1)}\right)^{1/2} \tag{4}$$

where ρ represents plasma mass densities (Cassak & Shay, 2007; Wang et al., 2015), before evaluating the reconnection onset condition derived by Doss et al. (2015), which is given as

$$\left|\frac{v_1 - v_2}{2}\right| < v_O \left(\frac{\rho_1 B_2 + \rho_2 B_1}{2(\rho_1 B_2 \rho_2 B_1)^{1/2}}\right) \tag{5}$$

We assume that reconnection onset is possible at points on the model magnetopause surface where all three conditions are satisfied. At all such points we can calculate the strength of the electric field that would result from onset (the reconnection rate) as

$$E = 2k\left(\frac{B_1 B_2}{B_1 + B_2}\right) v_O \left(1 - \frac{(v_1 - v_2)^2}{v_O^2} \frac{\rho_1 B_2 \rho_2 B_1}{(\rho_1 B_2 + \rho_2 B_1)^2}\right) \tag{6}$$

where k is the reconnection efficiency (the dimensionless reconnection rate). We set the efficiency as 0.1 to reflect observations of reconnection in near-Earth space (e.g., Paschmann et al., 2013), and in the present absence of evidence for a dependence of this efficiency on the absolute plasma β in the adjacent regimes that extends to the region of parameter space corresponding to Jupiter's magnetopause (Anderson et al., 1997; DiBraccio et al., 2013; Slavin & Holzer, 1979; Sonnerup, 1970). Note that the second bracketed term on the far right side of equation (6) captures the negative impact of bulk flow shears on the reconnection electric field strength, even under satisfaction of the related onset condition given in equation (5) (Doss et al., 2015).

Figure 4 shows an assessment of large-scale reconnection at Jupiter's magnetopause under the steady, typical near-magnetopause conditions presented in section 3. Figure 4a shows the magnetic shear across the model magnetopause, which is highest and lowest (antiparallel and parallel fields) in high-latitude flank regions of the surface for this typical IMF clock angle of 90°. Figure 4b shows the absolute difference in plasma β across the boundary, and the combination of these two derivatives of the model outputs allows us to apply the reconnection onset requirement related to diamagnetic particle drifts (equation (3)). Figure 4c shows the reconnection electric field strength in regions of the surface where all onset conditions are satisfied. These regions encompass the highest magnetic shears (Figure 4a), where the relative diamagnetic particle drift is closer to perpendicular to the direction of reconnection outflow (equation (3)), where the reconnecting magnetic field components are larger and so the outflows themselves are faster (equation (4)), where the flow shear is also approximately perpendicular to the outflow direction (Figures 2c and 3c and equation (5)), and thus also where the highest reconnection electric field strengths are found (equation (6)).

While reconnection is possible at all colored locations shown in Figure 4c, to estimate the voltage applied to Jupiter's magnetosphere

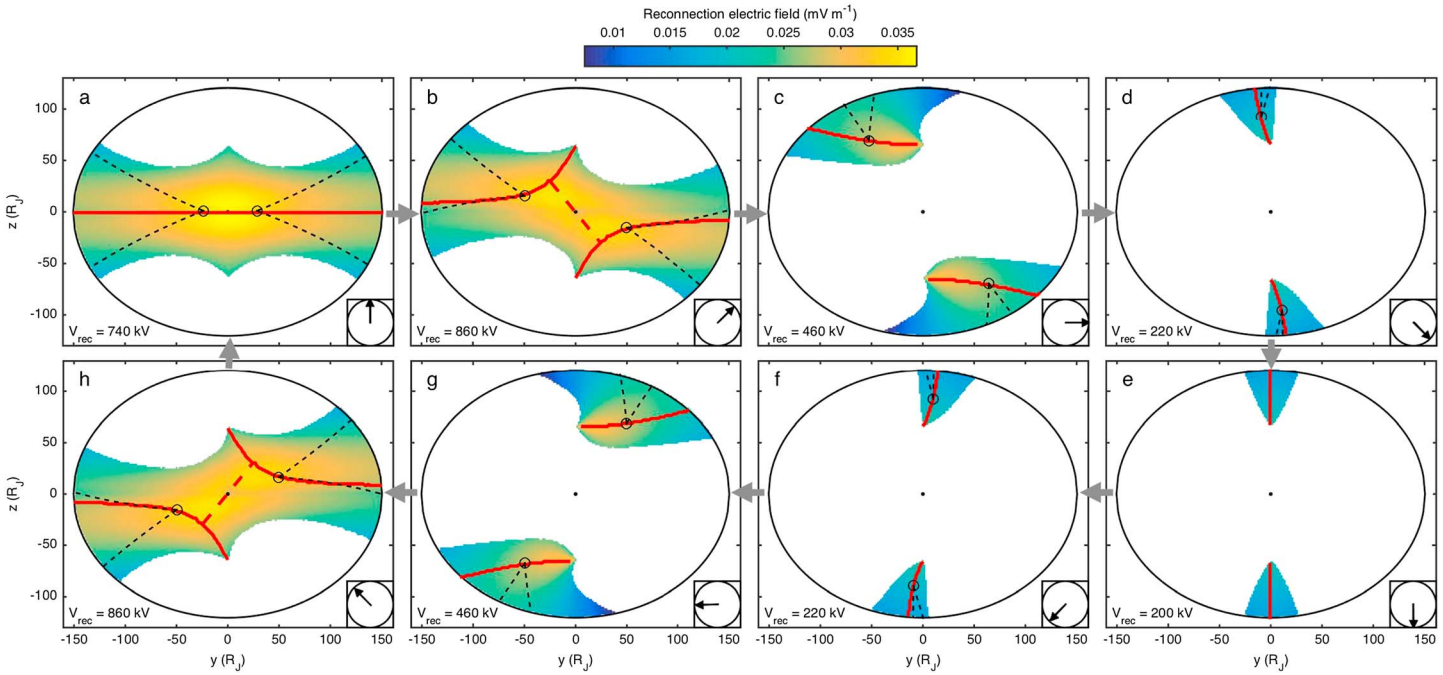

Figure 5. Assessments of steady state large-scale magnetic reconnection at Jupiter's magnetopause over a range of interplanetary magnetic field (IMF) clock angles, with all other inputs set to typical values in each case. In all panels the dayside model magnetopause surface is shown ($x > 0$) as viewed from the $-x$ direction (i.e., from the Sun; i.e., along the solar wind velocity vector), Jupiter is given as a black circle at the origin, and the IMF clock angle is indicated in the bottom right. In all panels color is only applied to regions where reconnection onset conditions are satisfied and indicate the reconnection electric field strength if reconnection were to occur locally. Solid red lines give the expected location of reconnection sites as the locus of points where the magnetic shear is 180°, assumed to be the reconnection X lines. Black circles give example locations on the X lines. Dashed lines approximate the paths taken by examples of plasma parcels in the reconnection outflow. Reconnection voltages (V_{rec}) are given in the bottom left.

by magnetopause reconnection, we follow the conventional approach that has been extensively applied to Earth's magnetopause (e.g., Trattner et al., 2007a). The red lines in Figure 4c describe the locus of points where the magnetic fields adjacent to the boundary are antiparallel, where we assume reconnection occurs at all points to form a reconnection X line. Integrating the reconnection electric field strength along each X line and summing leads to a dayside reconnection voltage, which is 460 kV (to two significant figures) in this case of typical conditions. This average voltage is of the same order of magnitude as previous estimates (e.g., Badman & Cowley, 2007); however, it is important to note that these modeling results rely on steady state conditions on a time scale that is not characteristic of the Jovian magnetosphere (see discussion later in this subsection).

The reconnection assessment shown in Figure 4c can also be used to approximate the motion of parcels of plasma in the reconnection inflow that pass close to the reconnection site and then form the reconnection outflow. The foundation of this tracking as competition between magnetosheath flow and magnetic tension forces associated with reconnected field lines was described by Cowley and Owen (1989) and has been applied to the magnetopauses of both Earth (Cooling et al., 2001) and Mercury (Slavin et al., 2012). Two predicted reconnection sites are chosen in Figure 4c (black circles), and the paths of two parcels of plasma across the model surface from each site are shown (dashed black lines).

We begin examining the sensitivity of large-scale magnetopause reconnection under steady state to model input values by isolating the effect of the IMF orientation. Figure 5 shows reconnection assessments (like that shown in Figure 4c) over the full range of clock angles, where all other model inputs are set as typical values (see Table 1). Under northward upstream solar wind magnetic field (Figure 5a) there is a high magnetic shear across the low-latitude magnetopause, producing a relatively long X line, high reconnection electric fields, and a reconnection voltage of 740 kV. Note that Figures 5b and 5h show cases where a single X line spanning the dayside magnetopause is possible, and indicated by dashed red lines (e.g., Trattner et al., 2007b). However, reconnection voltages given here are all based on antiparallel X lines (solid red lines only), since

the voltages in the two cases are the same when quoted to the level of accuracy used in Figure 5 (two significant figures).

As the upstream magnetic field rotates from northward to southward (Figures 5a through 5e) there is initially an increase in the voltage (Figure 5b). This is due to the sharp decrease of magnetospheric mass density with latitude (Figure 3a) that produces the strongest reconnection electric fields in regions just above and below the equator (e.g., Figure 5b and equations (4) through (6)), which the northward IMF X line passes between. With continuing rotation of the upstream magnetic field to southward (Figures 5b through 5e) the X line splits in two and moves to higher latitudes (with both X lines poleward of the cusps under near-southward IMF), and the reconnection electric field and voltage decrease. Figure 5c is the typical case shown in Figure 4c, and Figure 5g shows the results for the other prevailing clock angle of 270°, which are quantitatively similar (e.g., reconnection voltages).

The sensitivity of large-scale reconnection at Jupiter's magnetopause under steady state to all model inputs is indicated in Figure 6, focusing on reconnection voltages. The gray curve common to all panels is the dependence of the reconnection voltage on the IMF clock angle under typical near-magnetopause conditions (Figures 2–5). Most panels also indicate the impact of a 50% increase and a 50% decrease in a given typical model input as a red and blue curve, respectively. Reconnection voltages are most sensitive to upstream solar wind conditions, specifically, the strength of the IMF (Figure 6d) followed by the proton number density (Figure 6b). This is because these parameters control the typical Alfvén speed in the magnetosheath, which is more sensitive to changes in magnetic field strength than plasma mass density. The typical magnetosheath Alfvén speed at the magnetopause is lower than the typical magnetospheric Alfvén speed, which means that it primarily controls the strength of the reconnection electric field (equation (6)). Therefore, reconnection electric field strengths, and by extension the dayside reconnection voltage, are most sensitive to changes in the magnetosheath Alfvén speed, which produces the strongest responses in Figures 6b and 6d.

Changes in the level of magnetopause polar flattening affect the length of reconnection X lines and how these change with clock angle, while having little effect on the reconnection electric field strength, producing the differences between curves shown in Figure 6e. Realistic planetary magnetic dipole axis orientations are used in Figure 6f, which have a relatively small effect on the relationship between voltage and clock angle. The response to varying typical magnetospheric model inputs (Figures 6g through 6j) is considerably weaker than the response to changes in the upstream solar wind (Figures 6a through 6d), and similarly explained in terms of Alfvén speeds and the reconnection electric field. Note that the strongest magnetospheric response is to the plasma β (Figure 6i), which is anticorrelated with the magnetospheric Alfvén speed.

There are a number of issues to bear in mind when interpreting these modeling results. Perhaps the most important is the fact that the Jovian magnetosphere is rarely expected to be in steady state, since all model input parameters have either been shown to be or are expected to be functions of time (Ebert et al., 2014; Frank et al., 2002; Gruesbeck et al., 2017; Jackman & Arridge, 2011; Joy et al., 2002; Krupp et al., 2001). Particularly, relevant for magnetopause reconnection is the evidence that the typical time scale of IMF variability at Jupiter's orbit is considerably shorter than both the time taken for the unperturbed solar wind to travel a magnetopause standoff distance (~4 days), as well as the more significant and longer time taken for a change in the IMF immediately upstream of the subsolar bow shock to propagate through the slower magnetosheath flow regime and impact near-magnetopause conditions (Ebert et al., 2014; Gruesbeck et al., 2017; Jackman & Arridge, 2011; McComas & Bagenal, 2007). The more realistic picture of large-scale reconnection at Jupiter's magnetopause is therefore likely one where reconnection sites (X lines) are more mobile in response to relatively rapid changes in the upstream IMF and thus also where the reconnection voltages calculated here may be short-lived.

Another issue to consider is that our modeling assumes an initially "closed" magnetospheric magnetic field, that is, where there is no reconnected magnetic flux ("open" magnetic field lines) in the system. The presence of reconnected flux in the system could lead to reconnection poleward of the cusps (e.g., Figure 5e) that does not change the total amount of reconnected flux, and where the reconnection voltage may fall to zero. Furthermore, the operation of magnetopause reconnection itself will in turn affect other regions of the surface, resulting in layers of mixed plasma both internal and external to the boundary.

Bearing these issues in mind, the key conclusion concerning large-scale reconnection at the Jovian magnetopause that can be drawn based on the present modeling is that the location of reconnection sites, the

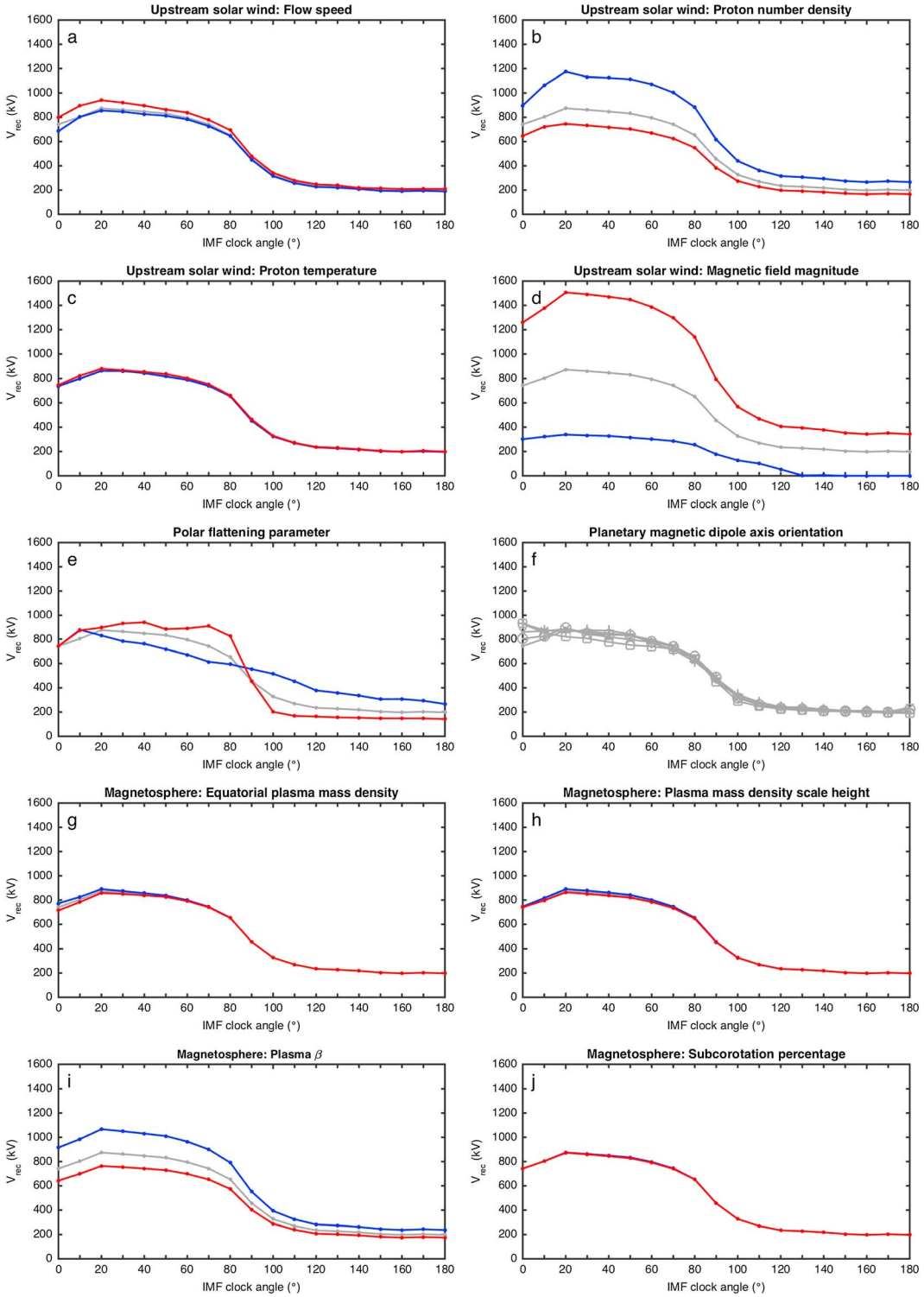

Figure 6. Relationships between the interplanetary magnetic field (IMF) clock angle and the dayside voltage applied to Jupiter's magnetopause due to steady state large-scale magnetopause reconnection over a range of conditions. In all panels where gray, red, and blue curves are shown the gray curve represents typical conditions, the red curve corresponds to a 50% increase of the input parameter in question, and the blue curve corresponds to a 50% decrease of the input parameter in question. (a) Upstream solar wind flow speed. (b) Upstream solar wind proton number density. (c) Upstream solar wind proton temperature. (d) Upstream solar wind magnetic field (IMF) magnitude. (e) Magnetopause polar flattening parameter. (f) Planetary magnetic dipole axis orientation, where the four gray curves with different markers correspond to rotations of the dipole axis about the rotation axis in 90° increments. (g) Magnetosphere equatorial mass density. (h) Magnetosphere plasma mass density scale height. (i) Magnetosphere plasma β. (j) Magnetosphere subcorotation percentage.

associated reconnection rates, and the resulting dayside reconnection voltage are all primarily controlled by the highly variable IMF, with a secondary role played by the similarly variable solar wind mass density. These assessments of large-scale reconnection at Jupiter's magnetopause should be viewed as an early step toward forming a global understanding of a complex phenomenon, and which must be reassessed in future to reflect our evolving understanding of reconnection microphysics (e.g., Burch et al., 2016). To give examples of added complexity to be considered in future work, reconnection sites are expected to move even under sub-Alfvénic flow conditions (Doss et al., 2015; Trenchi et al., 2015), and reconnection may occur at multiple locations within "reconnection-allowed" regions (e.g., Fuselier et al., 2017).

4.2. Kelvin-Helmholtz Instability

The starting point for a global assessment of K-H instability growth at the Jovian magnetopause under the steady near-magnetopause conditions predicted by the present modeling is the application of the classic condition for an interface between magnetized plasmas to be K-H unstable,

$$[\boldsymbol{k}\cdot(\boldsymbol{V}_2-\boldsymbol{V}_1)]^2 > \frac{1}{\mu_0}\left(\frac{1}{\rho_1}+\frac{1}{\rho_2}\right)\left[(\boldsymbol{k}\cdot\boldsymbol{B}_1)^2+(\boldsymbol{k}\cdot\boldsymbol{B}_2)^2\right] \tag{7}$$

where $\boldsymbol{k}$ is the wave vector, $\boldsymbol{V}$ is the plasma flow velocity, ρ represents the plasma mass density, $\boldsymbol{B}$ is the magnetic field vector, and the subscripts 1 and 2 indicate the near-magnetopause magnetosheath and magnetosphere, respectively. Favorable conditions for instability growth are therefore high flow shear, high mass densities, and adjacent magnetic fields that are perpendicular to the bulk flows, which limits the ability of magnetic tension to stabilize the interface.

To apply this condition, we consider all points on the model dayside magnetopause and then evaluate the left and right side of equation (7) for all choices of wave vector that are perpendicular to the local surface normal. If no choice of wave vector fulfills the K-H instability condition we conclude that the boundary is locally K-H stable; whereas, if any choice of wave vector does fulfill the condition then we conclude that the local boundary is K-H unstable. Note that the results presented and conclusions drawn in this subsection are the same if we set each local wave vector to be in the direction of the bulk flow shear.

The global assessment of K-H instability growth at Jupiter's magnetopause under steady, typical conditions (see section 3, Table 1, and Figures 2 and 3) is shown in Figure 7a. K-H stable regions of the model surface are shown in red and K-H unstable regions are shown in green. The K-H-unstable regions are located at low latitudes, where flow shears are approximately perpendicular to the magnetospheric magnetic field (Figures 2c, 2d, 3c, and 3d), limiting the associated stabilization of the interface via magnetic tension forces. In the case of corotation-dominated systems like the Jovian magnetosphere the cross-magnetopause flow shear is also highest in the low-latitude region and shows a strong dawn-dusk asymmetry (Figures 2c and 3c). This produces a typically K-H unstable low-latitude magnetopause at dawn, compared to a typically stable duskside (Figure 7a). Note that the low-latitude dusk magnetopause close to the terminator is K-H unstable due to the acceleration of the magnetosheath flow away from the subsolar point that eventually surpasses the speed of subcorotating magnetospheric plasma.

The remaining panels in Figure 7 test the sensitivity of this picture of K-H unstable and K-H stable regions to changes in the upstream solar wind inputs to the model. Similar to the assessments of large-scale reconnection presented in section 4.1, we carry out these sensitivity tests by increasing and decreasing each input by 50%, while all other parameters are typical, and repeating the K-H instability assessment. An exception to this approach is Figure 7b, where the IMF orientation has been set to southward (with all other parameters typical) in order to be compared with the typical K-H instability assessment (Figure 7a) and reveal the impact of the magnetosheath magnetic field direction. This comparison shows larger K-H unstable regions under southward IMF (and equivalently also northward IMF, see equation (7)), which is the result of the magnetosheath magnetic field also being ineffective at stabilizing the low-latitude boundary via magnetic tension in this case. Note that the rotation of the low-latitude magnetosheath magnetic toward northward/southward for IMF orientations between typical and southward/northward enhances this effect (see supporting information). The stabilizing influence of magnetic tension is also responsible for the anticorrelation between the size of K-H unstable regions and the strength of the IMF (Figures 7c and 7d). Under weaker magnetosheath magnetic field conditions the K-H unstable regions form a single, continuous region across the low-latitude magnetopause (Figure 7d).

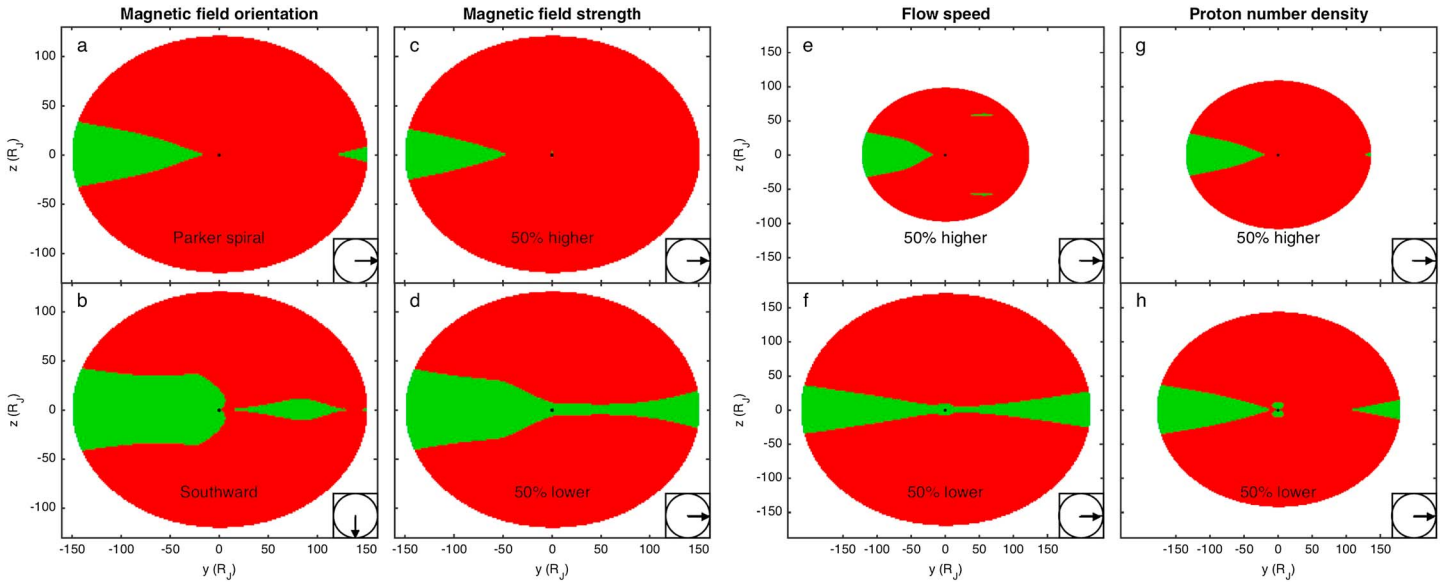

Figure 7. Assessments of Kelvin-Helmholtz (K-H) instability growth at Jupiter's magnetopause under steady state: Dependence of K-H unstable regions on upstream solar wind input parameters to the model. In all panels the dayside model magnetopause surface is shown ($x > 0$) as viewed from the $-x$ direction (i.e., from the Sun; i.e., along the solar wind velocity vector), and Jupiter is given as a black circle at the origin. Red color indicates regions where the boundary is locally K-H stable at all points, whereas green color indicates regions where the boundary is locally K-H unstable at all points. The interplanetary magnetic field (IMF) orientation is shown in the bottom right of each panel. All input parameters are set to typical values unless stated. (a) K-H instability assessment under typical conditions. (b) K-H instability assessment under southward IMF. (c) K-H instability assessment with 50% stronger IMF. (d) K-H instability assessment with 50% weaker IMF. (e) K-H instability assessment with 50% higher upstream solar wind flow speed. (f) K-H instability assessment with 50% lower upstream solar wind flow speed. (g) K-H instability assessment with 50% higher upstream solar wind proton number density. (h) K-H instability assessment with 50% lower upstream solar wind proton number density.

The impact of changing the upstream solar wind flow speed and proton number (mass) density is more difficult to assess with our modeling approach, since these change the solar wind dynamic pressure and thus the scale of the model magnetopause surface, which in turn affects magnetospheric conditions (see section 2). More specifically, since we do not include a dependence of the magnetospheric subcorotation percentage on the dynamic pressure of the solar wind (see section 2 and Table 1) the magnetospheric flow speeds are considerably higher for more expanded magnetospheres (Figures 7f and 7h). In the absence of a more detailed framework that describes the response of the near-magnetopause magnetospheric plasma flow to changing solar wind dynamic pressure on different time scales, we can only state that we expect both higher upstream solar wind flow speed and higher proton number density to promote magnetopause K-H instability (see equation (7)).

The sensitivity of the typical assessment of K-H instability at Jupiter's magnetopause to variations in the magnetospheric model inputs (Table 1) is similarly explored in Figure 8. The impact of increasing and decreasing the equatorial plasma mass density (a proxy for the mass of the dayside plasma sheet) is as expected based on inspection of equation (7) (Figures 8a and 8b). Higher magnetospheric plasma mass densities at the magnetopause lead to larger K-H-unstable regions, and vice versa under lower density conditions. Similarly, higher input mass density scale height, (effectively a thicker dayside plasma sheet) also promotes boundary K-H instability (Figure 8c), in contrast to the case of lower scale height (Figure 8d).

The response to the input magnetospheric plasma β (Figures 8e and 8f) explores the impact of stronger and weaker magnetospheric magnetic fields. This is because the model maintains total pressure balance with the external magnetosheath solar wind at all points and sets the value of both the magnetospheric magnetic field strength and the total plasma pressure to enforce the required plasma β locally (see section 2). Figure 8e therefore corresponds to lower than typical magnetic field strengths, whereas Figure 8f corresponds to higher than typical magnetic field strengths, and K-H unstable regions are slightly larger in the former case than the latter as expected (equation (7)). Note that a more modest change in the magnetospheric magnetic field strength than 50% is required to produce a 50% change in the plasma β. Figures 8g and 8h show the response to the subcorotation percentage, which dictates the speed of magnetospheric plasma

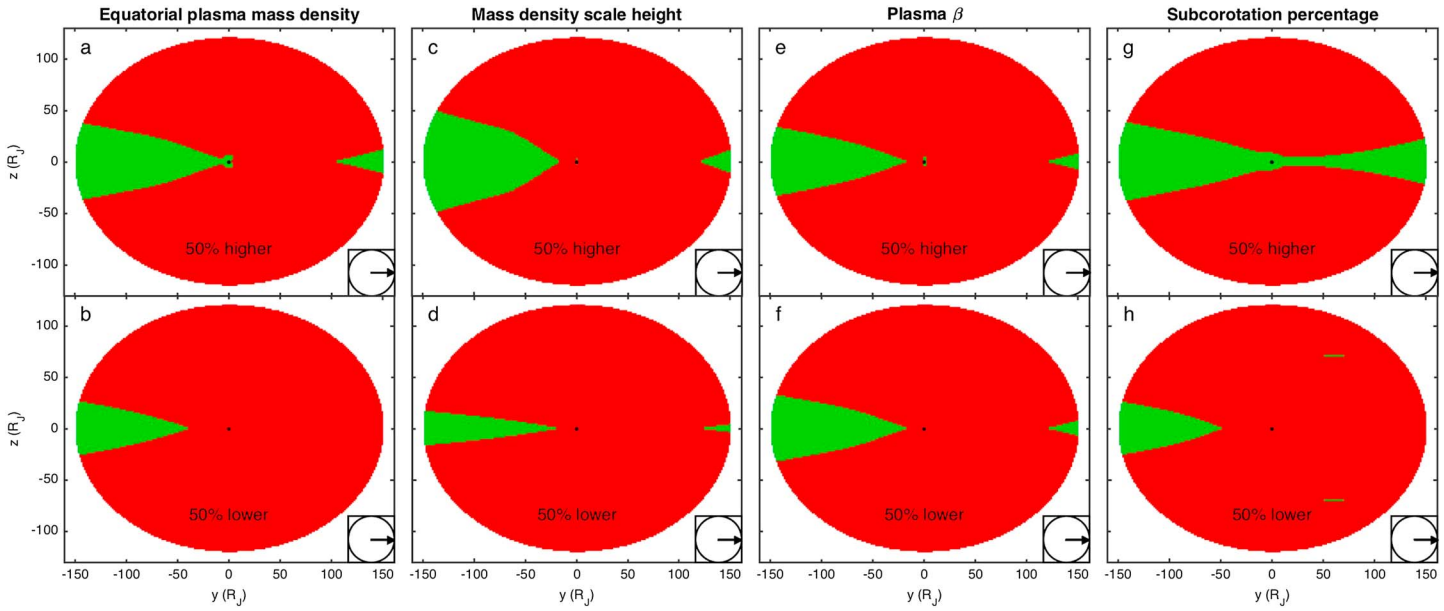

Figure 8. Assessments of Kelvin-Helmholtz (K-H) instability growth at Jupiter's magnetopause under steady state: Dependence of K-H unstable regions on magnetosphere input parameters to the model. In all panels the dayside model magnetopause surface is shown ($x > 0$) as viewed from the $-x$ direction (i.e., from the Sun; i.e., along the solar wind velocity vector), and Jupiter is given as a black circle at the origin. Red color indicates regions where the boundary is locally K-H stable at all points, whereas green color indicates regions where the boundary is locally K-H unstable at all points. The interplanetary magnetic field orientation is shown in the bottom right of each panel. All input parameters are set to typical values unless stated. (a) K-H instability assessment with 50% higher magnetosphere equatorial plasma mass density. (b) K-H instability assessment with 50% lower magnetosphere equatorial plasma mass density. (c) K-H instability assessment with 50% higher magnetosphere plasma mass density scale height. (d) K-H instability assessment with 50% lower magnetosphere plasma mass density scale height. (e) K-H instability assessment with 50% higher magnetosphere plasma β. (f) K-H instability assessment with 50% lower magnetosphere plasma β. (g) K-H instability assessment with 50% higher magnetosphere subcorotation percentage. (h) K-H instability assessment with 50% lower magnetosphere subcorotation percentage.

flow. Higher flow speeds lead to higher flow shears across the model magnetopause and larger K-H unstable regions. Figure 8g shows another case where using an atypical model input produces a K-H-unstable region that spans the low-latitude dayside boundary.

Our assessments of K-H instability growth at Jupiter's magnetopause have so far focused on predicting the regions of the surface where the boundary is locally unstable to perturbation. Such perturbations in K-H unstable regions will grow and evolve over time, propagating with the local velocity of the zero-momentum (center-of-mass) frame. This path taken by K-H boundary perturbations can be explored with the modeling framework. The velocity of the zero-momentum frame under typical model inputs is shown in Figure 9a. The lowest frame speeds are found in the low-latitude regions where the magnetosheath flow speeds are lower and where the magnetosheath and magnetospheric flows are approximately antiparallel to each other (Figures 2c and 3c). Note that while the momentum of the magnetosheath flow tends to dominate the zero-momentum frame, the momentum of subcorotating magnetospheric plasma is responsible for the dawn-dusk direction of the zero-momentum frame at the subsolar point. In Figure 9b the input magnetospheric equatorial mass density, scale height, and subcorotation percentage have all been increased by 50% to highlight this effect.

These zero-momentum frame velocities are the expected velocities of K-H boundary perturbations. Therefore, for a given K-H-unstable point on the model magnetopause the motion of a perturbation can be tracked from this origin to where it leaves the dayside. This is a similar model capability to the tracking of parcels of plasma on reconnected magnetic field lines described and demonstrated in section 4.1. While such perturbations are driven in K-H-unstable regions, it is important to note that they can propagate away from such regions, in to regions where the boundary is locally stable. Consequently, the largest K-H boundary perturbations (e.g., vortices) will not necessarily be encountered in the regions where the magnetopause is locally unstable.

Similar to our assessments of large-scale reconnection, it is important to note that these assessments of K-H instability at Jupiter's magnetopause are also based on steady state modeling of a system that is expected to

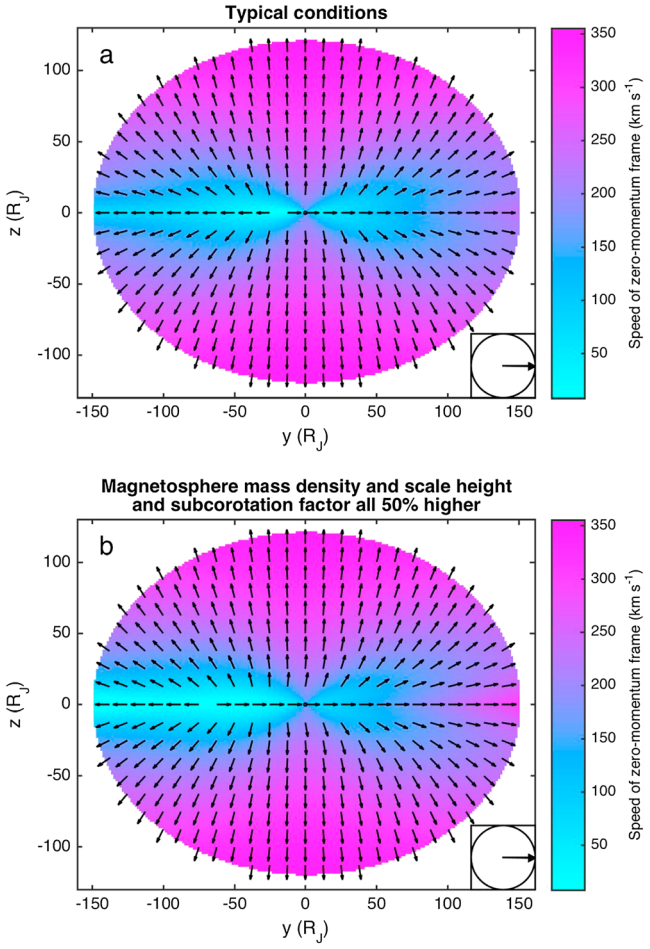

Figure 9. Velocity of K-H perturbations of Jupiter's magnetopause boundary under steady state conditions, given as the local velocity of the zero-momentum reference frame. In both panels the dayside model magnetopause surface is shown ($x > 0$) as viewed from the $-x$ direction (i.e., from the Sun; i.e., along the solar wind velocity vector), and Jupiter is given as a black circle at the origin. The interplanetary magnetic field orientation is shown in the bottom right of each panel. All input parameters are set to typical values unless stated. Color applied to the surface indicates the local speed of the zero-momentum frame, and black arrows indicate its velocity. (a) Velocity of K-H perturbations under typical conditions. (b) Velocity of K-H perturbations with magnetosphere equatorial mass density, mass density scale height, and subcorotation percentage all increased by 50%.

typically not be in steady state (see discussion in section 4.1). However, in contrast to the large-scale reconnection results the K-H instability results presented in this subsection suggest that the operation of this process at Jupiter's magnetopause is less sensitive to changes in near-magnetopause conditions. Specifically, the equatorial dawn region of K-H instability persists in all scenarios shown in Figures 7 and 8. Coupling of Jupiter's magnetosphere to the solar wind via the operation of this process (quantified by the resulting voltage applied to the system, discussed below) may therefore be more stable with time than the coupling resulting from large-scale reconnection.

The growth of the K-H instability at Jupiter's magnetopause assessed in this subsection is capable of allowing mass transport across a planetary magnetopause. The process is therefore also a candidate mechanism for producing adjacent boundary layers of mixed plasma, where the inner edge of the resulting internal boundary layer itself can potentially become K-H unstable (Ogilvie & Fitzenreiter, 1989). K-H waves and rolled-up K-H vortices are thought to produce this significant cross-magnetopause transport (e.g., Fujimoto & Terasawa, 1994; Hasegawa et al., 2004; Ma et al., 2017 and are capable of twisting magnetic field lines to induce local (small scale) magnetic reconnection both within the structure and potentially also at magnetically conjugate locations at higher latitudes (Eriksson et al., 2016; Hasegawa et al., 2009; Nakamura et al., 2013; Ma et al., 2014a, 2014b; Ma et al., 2017; Nikutowski et al., 2002; Nykyri et al., 2006). The possibility of local, intermittent opening and closing of magnetic field lines and associated mass transport due to K-H vortices has been proposed in the literature (see discussion in Delamere & Bagenal, 2010, and Burkholder et al., 2017). The voltage applied to the system due to this "viscous-like" interaction involving K-H instability growth at the magnetopause is difficult to constrain, and not quantified in the present study. If constrained in future then a comparison with the voltage arising from large-scale magnetopause reconnection (see section 4.1) would reveal the dominant external driver of Jupiter's magnetosphere.

Recent work based on numerical modeling and spacecraft observations at Saturn suggest/show that the most dramatic K-H-driven boundary perturbation (i.e., vortices) are more frequently encountered on the dusk flank of magnetospheres where near-magnetopause magnetospheric plasma subcorotates with the planet (Delamere et al., 2013; Ma et al., 2015; Masters et al., 2012). The present modeling results concerning regions of K-H instability and the subsequent motion of K-H perturbations support this expectation (Figures 7–9). Note that K-H vortices are evolving structures, the spatial scale of which at a particular time and location of encounter is a function of a number of parameters.

5. Summary

In this paper we have used an analytical modeling approach to shed light on the operation of key processes at Jupiter's dayside magnetopause under a wide range of steady state conditions. The model predicts magnetized plasma conditions immediately adjacent to the boundary based on specified input parameters (upstream solar wind and magnetosphere), which allow the operation of both large-scale magnetic reconnection and growth of the K-H instability to be assessed. We draw the following conclusions based on the present modeling:

1. Magnetic reconnection at Jupiter's magnetopause is most sensitive to the IMF, followed by the solar wind mass density.

2. The typical voltage applied to Jupiter's magnetosphere by large-scale magnetopause reconnection under steady state conditions is ~500 kV, but such steady state conditions are not expected to be common.
3. Regions of Jupiter's magnetopause that are unstable to growth of the K-H instability are less sensitive to changing conditions, and K-H perturbations can move from dawn to dusk across the subsolar region.
4. The voltage applied to Jupiter's magnetosphere by the "viscous-like" interaction involving K-H instability remains unclear and is needed to reveal the dominant solar wind influence.

This modeling represents an early yet crucial step in revealing how Jupiter's magnetosphere interacts with the solar wind. In future the present model will be tested with new in situ spacecraft observations and can be used to investigate the interplay between different boundary processes. Where appropriate, the model can be used to provide context for both local magnetopause observations and remote auroral observations, allowing potentially important tests of both our fundamental understanding of space plasma processes and our evolving picture of how the Jovian magnetospheric system works.

Acknowledgments
A. M. is supported by a Royal Society University Research Fellowship and thanks the International Space Science Institute for their support through selection of team number 357 "How does the Solar Wind Influence the Giant Planet Magnetospheres?" Please direct data requests to Adam Masters (a.masters@imperial.ac.uk).

References

Anderson, B. J., Phan, T.-D., & Fuselier, S. A. (1997). Relationships between plasma depletion and subsolar reconnection. *Journal of Geophysical Research*, *102*(A5), 9531–9542. https://doi.org/10.1029/97JA00173

Badman, S. V., Bonfond, B., Fujimoto, M., Gray, R. L., Kasaba, Y., Kasahara, S., … Yoshioka, K. (2016). Weakening of Jupiter's main auroral emission during January 2014. *Geophysical Research Letters*, *43*, 988–997. https://doi.org/10.1002/2015GL067366

Badman, S. V., & Cowley, S. W. H. (2007). Significance of Dungey-cycle flows in Jupiter's and Saturn's magnetospheres, and their identification on closed equatorial field lines. *Annales de Geophysique*, *25*(4), 941–951. https://doi.org/10.5194/angeo-25-941-2007

Bagenal, F., Adriani, A., Allegrini, F., Bolton, S. J., Bonfond, B., Bunce, E. J., … Zarka, P. (2014). Magnetospheric science objectives of the Juno mission. *Space Science Reviews*, 1–69. https://doi.org/10.1007/s11214-014-0036-8

Bagenal, F., & Delamere, P. A. (2011). Flow of mass and energy in the magnetospheres of Jupiter and Saturn. *Journal of Geophysical Research*, *116*, A05209. https://doi.org/10.1029/2010JA016294

Bagenal, F., Dowling, T. E., & McKinnon, W. B. (Eds.) (2004). *Jupiter: The Planet, Satellites, and Magnetosphere*. Cambridge, UK: Cambridge University Press.

Bagenal, F., Wilson, R. J., Siler, S., Paterson, W. R., & Kurth, W. S. (2016). Survey of Galileo plasma observations in Jupiter's plasma sheet. *Journal of Geophysical Research: Planets*, *121*, 871–894. https://doi.org/10.1002/2016JE005009

Baron, R. L., Owen, T., Connerney, J. E. P., Satoh, T., & Harrington, J. (1996). Solar wind control of Jupiter's H3+ auroras. *Icarus*, *120*(2), 437–442. https://doi.org/10.1006/icar.1996.0063

Barrow, C. H. (1978). Jupiter's decametric radio emission and solar activity. *Planetary and Space Science*, *26*(12), 1193–1199. https://doi.org/10.1016/0032-0633(78)90059-4

Barrow, C. H. (1979). Association of corotating magnetic sector structure with Jupiter's decameter-wave radio emission. *Journal of Geophysical Research*, *84*(A9), 5366–5372. https://doi.org/10.1029/JA084iA09p05366

Barrow, C. H., Genova, F., & Desch, M. D. (1986). Solar wind control of Jupiter's decametric radio emission. *Astronomy and Astrophysics*, *165*, 244–250.

Burch, J. L., Torbert, R. B., Phan, T. D., Chen, L. J., Moore, T. E., Ergun, R. E., … Chandler, M. (2016). Electron-scale measurements of magnetic reconnection in space. *Science*, *352*(6290), aaf2939. https://doi.org/10.1126/science.aaf2939

Burkholder, B., Delamere, P. A., Ma, X., Thomsen, M. F., Wilson, R. J., & Bagenal, F. (2017). Local time asymmetry of Saturn's magnetosheath flows. *Geophysical Research Letters*, *44*, 5877–5883. https://doi.org/10.1002/2017GL073031

Cassak, P. A., & Otto, A. (2011). Scaling of the magnetic reconnection rate with symmetric shear flow. *Physics of Plasmas*, *18*, 074501. https://doi.org/10.1063/1.3609771

Cassak, P. A., & Shay, M. A. (2007). Scaling of asymmetric magnetic reconnection: General theory and collisional simulations. *Physics of Plasmas*, *14*, 102114. https://doi.org/10.1063/1.2795630(10), 102114.

Chané, E., Saur, J., Keppens, R., & Poedts, S. (2017). How is the Jovian main auroral emission affected by the solar wind? *Journal of Geophysical Research: Space Physics*, *122*, 1960–1978. https://doi.org/10.1002/2016JA023318

Clarke, J. T., Nichols, J., Gérard, J.-C., Grodent, D., Hansen, K. C., Kurth, W., … Cecconi, B. (2009). Response of Jupiter's and Saturn's auroral activity to the solar wind. *Journal of Geophysical Research*, *114*, A05210. https://doi.org/10.1029/2008JA013694

Cooling, B. M. A., Owen, C. J., & Schwartz, S. J. (2001). Role of magnetosheath flow in determining the motion of open flux tubes. *Journal of Geophysical Research*, *106*(A9), 18,763–18,775. https://doi.org/10.1029/2000JA000455

Cowley, S. W. H., & Bunce, E. J. (2001). Origin of the main auroral oval in Jupiter's coupled magnetosphere-ionosphere system. *Planetary and Space Science*, *49*(10-11), 1067–1088. https://doi.org/10.1016/S0032-0633(00)00167-7

Cowley, S. W. H., & Bunce, E. J. (2003). Modulation of Jupiter's main auroral oval emissions by solar wind induced expansions and compressions of the magnetosphere. *Planetary and Space Science*, *51*(1), 57–79. https://doi.org/10.1016/S0032-0633(02)00118-6

Cowley, S. W. H., & Owen, C. J. (1989). A simple illustrative model of open flux tube motion over the dayside magnetopause. *Planetary and Space Science*, *37*(11), 1461–1475. https://doi.org/10.1016/0032-0633(89)90116-5

Crooker, N. U. (1979). Dayside merging and cusp geometry. *Journal of Geophysical Research*, *84*(A3), 951–959. https://doi.org/10.1029/JA084iA03p00951

Delamere, P. A., & Bagenal, F. (2010). Solar wind interaction with Jupiter's magnetosphere. *Journal of Geophysical Research*, *115*, A10201. https://doi.org/10.1029/2010JA015347

Delamere, P. A., & Bagenal, F. (2013). Magnetotail structure of the giant magnetospheres: Implications of the viscous interaction with the solar wind. *Journal of Geophysical Research: Space Physics*, *118*, 7045–7053. https://doi.org/10.1002/2013JA019179

Delamere, P. A., Wilson, R. J., Eriksson, S., & Bagenal, F. (2013). Magnetic signatures of Kelvin-Helmholtz vortices on Saturn's magnetopause: Global survey. *Journal of Geophysical Research: Space Physics*, *118*, 393–404. https://doi.org/10.1029/2012JA018197

Desroche, M., Bagenal, F., Delamere, P. A., & Erkaev, N. (2012). Conditions at the expanded Jovian magnetopause and implications for the solar wind interaction. *Journal of Geophysical Research*, *117*, A07202. https://doi.org/10.1029/2012JA017621

Dessler, A. J. (1983). *Physics of the Jovian Magnetosphere*. Cambridge, UK: Cambridge University Press. https://doi.org/10.1017/CBO9780511564574

DiBraccio, G. A., Slavin, J. A., Boardsen, S. A., Anderson, B. J., Korth, H., Zurbuchen, T. H., … Solomon, S. C. (2013). MESSENGER observations of magnetopause structure and dynamics at Mercury. *Journal of Geophysical Research: Space Physics*, *118*, 997–1008. https://doi.org/10.1002/jgra.50123

Doss, C. E., Komar, C. M., Cassak, P. A., Wilder, F. D., Eriksson, S., & Drake, J. F. (2015). Asymmetric magnetic reconnection with a flow shear and applications to the magnetopause. *Journal of Geophysical Research: Space Physics*, *120*, 7748–7763. https://doi.org/10.1002/2015JA021489

Dungey, J. W. (1961). Interplanetary magnetic field and the auroral zones. *Physical Review Letters*, *6*(2), 47–48. https://doi.org/10.1103/PhysRevLett.6.47

Dunlop, M. W., Zhang, Q.-H., Bogdanova, Y. V., Trattner, K. J., Pu, Z., Hasegawa, H., … Carr, C. M. (2011). Magnetopause reconnection across wide local time. *Annales de Geophysique*, *29*(9), 1683–1697. https://doi.org/10.5194/angeo-29-1683-2011

Dunn, W. R., Branduardi-Raymont, G., Elsner, R. F., Vogt, M. F., Lamy, L., Ford, P. G., … Jasinski, J. M. (2016). The impact of an ICME on the Jovian X-ray aurora. *Journal of Geophysical Research: Space Physics*, *121*, 2274–2307. https://doi.org/10.1002/2015JA021888

Ebert, R. W., Allegrini, F., Bagenal, F., Bolton, S. J., Connerney, J. E. P., Clark, G., … Wilson, R. J. (2017). Accelerated flows at Jupiter's magnetopause: Evidence for magnetic reconnection along the dawn flank. *Geophysical Research Letters*, *44*, 4401–4409. https://doi.org/10.1002/2016GL072187

Ebert, R., Bagenal, F., McComas, D., & Fowler, C. (2014). A survey of solar wind conditions at 5 AU: A tool for interpreting solar wind-magnetosphere interactions at Jupiter. *Frontiers in Astronomy and Space Sciences*, *1*, 4. https://doi.org/10.3389/fspas.2014.00004

Ebert, R. W., McComas, D. J., Bagenal, F., & Elliott, H. A. (2010). Location, structure, and motion of Jupiter's dusk magnetospheric boundary from ~1625 to 2550 RJ. *Journal of Geophysical Research*, *115*, A12223. https://doi.org/10.1029/2010JA015938

Echer, E., Zarka, P., Gonzalez, W. D., Morioka, A., & Denis, L. (2010). Solar wind effects on Jupiter non-Io DAM emissions during Ulysses distant encounter (2003–2004). *Astronomy and Astrophysics*, *519*, A84. https://doi.org/10.1051/0004-6361/200913305, A84

Eriksson, S., Lavraud, B., Wilder, F. D., Stawarz, J. E., Giles, B. L., Burch, J. L., … Goodrich, K. A. (2016). Magnetospheric multiscale observations of magnetic reconnection associated with Kelvin-Helmholtz waves. *Geophysical Research Letters*, *43*, 5606–5615. https://doi.org/10.1002/2016GL068783

Erkaev, N. V., Farrugia, C. J., & Biernat, H. K. (1996). Effects on the Jovian magnetosheath arising from solar wind flow around nonaxisymmetric bodies. *Journal of Geophysical Research*, *101*(A5), 10,665–10,672. https://doi.org/10.1029/95JA03518

Farrugia, C. J., Biernat, H. K., & Erkaev, N. V. (1998). The effect of the magnetopause shapes of Jupiter and Saturn on magnetosheath parameters. *Planetary and Space Science*, *46*(5), 507–514. https://doi.org/10.1016/S0032-0633(97)00225-0

Frank, L. A., Paterson, W. R., & Khurana, K. K. (2002). Observations of thermal plasma in Jupiter's magnetotail. *Journal of Geophysical Research*, *107*(A1), 1003. https://doi.org/10.1029/2001JA000077

Fujimoto, M., & Terasawa, T. (1994). Anomalous ion mixing within an MHD scale Kelvin-Helmholtz vortex. *Journal of Geophysical Research*, *99*(A5), 8601–8613, https://doi.org/10.1029/93JA02722

Fuselier, S. A., Burch, J. L., Cassak, P. A., Goldstein, J., Gomez, R. G., Goodrich, K., … Valek, P. (2016). Magnetospheric ion influence on magnetic reconnection at the duskside magnetopause. *Geophysical Research Letters*, *43*, 1435–1442. https://doi.org/10.1002/2015GL067358

Fuselier, S. A., Trattner, K. J., & Petrinec, S. M. (2011). Anti-parallel and component reconnection at the dayside magnetopause. *Journal of Geophysical Research*, *116*, A10227. https://doi.org/10.1029/2011JA016888

Fuselier, S. A., Vines, S. K., Burch, J. L., Petrinec, S. M., Trattner, K. J., Cassak, P. A., … Webster, J. M. (2017). Large-scale characteristics of reconnection diffusion regions and associated magnetopause crossings observed by MMS. *Journal of Geophysical Research: Space Physics*, *122*, 5466–5486. https://doi.org/10.1002/2017JA024024

Galopeau, P. H. M., & Boudjada, M. Y. (2005). Solar wind control of Jovian auroral emissions. *Journal of Geophysical Research*, *110*, A09221. https://doi.org/10.1029/2004JA010843

Genova, F., Zarka, P., & Barrow, C. H. (1987). Voyager and Nancay observations of the Jovian radio-emission at different frequencies—Solar wind effect and source extent. *Astronomy and Astrophysics*, *182*, 159–162.

Gershman, D. J., DiBraccio, G. A., Connerney, J. E. P., Hospodarsky, G., Kurth, W. S., Ebert, R. W., … Bolton, S. J. (2017). Juno observations of large-scale compressions of Jupiter's dawnside magnetopause. *Geophysical Research Letters*, *44*, 7559–7568. https://doi.org/10.1002/2017GL073132

Gomez, R. G., Vines, S. K., Fuselier, S. A., Cassak, P. A., Strangeway, R. J., Petrinec, S. M., … Mukherjee, J. (2016). Stable reconnection at the dusk flank magnetopause. *Geophysical Research Letters*, *43*, 9374–9382. https://doi.org/10.1002/2016GL069692

Grodent, D., Clarke, J. T., Kim, J., Waite, J. H. Jr., & Cowley, S. W. H. (2003). JJupiter's main auroral oval observed with HST-STIS. *Journal of Geophysical Research*, *108*(A11), 1389. https://doi.org/10.1029/2003JA009921

Gruesbeck, J. R., Gershman, D. J., Espley, J. R., & Connerney, J. E. P. (2017). The interplanetary magnetic field observed by Juno enroute to Jupiter. *Geophysical Research Letters*, *44*, 5936–5942. https://doi.org/10.1002/2017GL073137

Gurnett, D. A., Kurth, W. S., Hospodarsky, G. B., Persoon, A. M., Zarka, P., Lecacheux, A., … Dougherty, M. K. (2002). Control of Jupiter's radio emission and aurorae by the solar wind. *Nature*, *415*(6875), 985–987. https://doi.org/10.1038/415985a

Hasegawa, H., Fujimoto, M., Phan, T.-D., Rème, H., Balogh, A., Dunlop, M. W., … TanDokoro, R. (2004). Transport of solar wind into Earth's magnetosphere through rolled-up Kelvin-Helmholtz vortices. *Nature*, *430*(7001), 755–758. https://doi.org/10.1038/nature02799

Hasegawa, H., Retinó, A., Vaivads, A., Khotyaintsev, Y., André, M., Nakamura, T. K. M., … Canu, P. (2009). Kelvin-Helmholtz waves at the Earth's magnetopause: Multiscale development and associated reconnection. *Journal of Geophysical Research*, *114*, A12207. https://doi.org/10.1029/2009JA014042

Hess, S. L. G., Echer, E., & Zarka, P. (2012). Solar wind pressure effects on Jupiter decametric radio emissions independent of Io. *Planetary and Space Science*, *70*(1), 114–125. https://doi.org/10.1016/j.pss.2012.05.011

Hess, S. L. G., Echer, E., Zarka, P., Lamy, L., & Delamere, P. A. (2014). Multi-instrument study of the Jovian radio emissions triggered by solar wind shocks and inferred magnetospheric subcorotation rates. *Planetary and Space Science*, *99*, 136–148. https://doi.org/10.1016/j.pss.2014.05.015

Hospodarsky, G. B., Kurth, W. S., Allegrini, F., Bolton, S. J., Clark, G. B., Connerney, J. E. P., … McComas, D. J. (2017). Jovian bow shock and magnetopause encounters by the Juno spacecraft. *Geophysical Research Letters*, *44*, 4506–4512. https://doi.org/10.1002/2017GL073177

Huddleston, D. E., Russell, C. T., Kivelson, M. G., Khurana, K. K., & Bennett, L. (1998). Location and shape of the Jovian magnetopause and bow shock. *Journal of Geophysical Research*, *103*(E9), 20,075–20,082. https://doi.org/10.1029/98JE00394

Huddleston, D. E., Russell, C. T., Le, G., & Szabo, A. (1997). Magnetopause structure and the role of reconnection at the outer planets. *Journal of Geophysical Research*, *102*(A11), 24,289–24,302. https://doi.org/10.1029/97JA02416

Jackman, C. M., & Arridge, C. S. (2011). Solar cycle effects on the dynamics of Jupiter's and Saturn's magnetospheres. *Solar Physics*, *274*(1-2), 481–502. https://doi.org/10.1007/s11207-011-9748-z

Joy, S. P., Kivelson, M. G., Walker, R. J., Khurana, K. K., Russell, C. T., & Ogino, T. (2002). Probabilistic models of the Jovian magnetopause and bow shock locations. *Journal of Geophysical Research*, *107*(A10), 1309. https://doi.org/10.1029/2001JA009146

Kaiser, M. L. (1993). Time-variable magnetospheric radio emissions from Jupiter. *Journal of Geophysical Research*, *98*(E10), 18,757–18,765. https://doi.org/10.1029/93JE01279

Khurana, K. K. (2001). Influence of solar wind on Jupiter's magnetosphere deduced from currents in the equatorial plane. *Journal of Geophysical Research*, *106*(A11), 25,999–26,016. https://doi.org/10.1029/2000JA000352

Kimura, T., Badman, S. V., Tao, C., Yoshioka, K., Murakami, G., Yamazaki, A., … Clarke, J. T. (2015). Transient internally driven aurora at Jupiter discovered by Hisaki and the Hubble Space Telescope. *Geophysical Research Letters*, *42*, 1662–1668. https://doi.org/10.1002/2015GL063272

Kimura, T., Kraft, R. P., Elsner, R. F., Branduardi-Raymont, G., Gladstone, G. R., Tao, C., … Murray, S. S. (2016). Jupiter's X-ray and EUV auroras monitored by Chandra, XMM-Newton, and Hisaki satellite. *Journal of Geophysical Research: Space Physics*, *121*, 2308–2320. https://doi.org/10.1002/2015JA021893

Kita, H., Kimura, T., Tao, C., Tsuchiya, F., Misawa, H., Sakanoi, T., … Fujimoto, M. (2016). Characteristics of solar wind control on Jovian UV auroral activity deciphered by long-term Hisaki EXCEED observations: Evidence of preconditioning of the magnetosphere? *Geophysical Research Letters*, *43*, 6790–6798. https://doi.org/10.1002/2016GL069481

Kobel, E., & Flückiger, E. O. (1994). A model of the steady state magnetic field in the magnetosheath. *Journal of Geophysical Research*, *99*(A12), 23,617–23,622. https://doi.org/10.1029/94JA01778

Komar, C. M., Fermo, R. L., & Cassak, P. A. (2015). Comparative analysis of dayside magnetic reconnection models in global magnetosphere simulations. *Journal of Geophysical Research: Space Physics*, *120*, 276–294. https://doi.org/10.1002/2014JA020587

Krupp, N., Lagg, A., Livi, S., Wilken, B., Woch, J., Roelof, E. C., & Williams, D. J. (2001). Global flows of energetic ions in Jupiter's equatorial plane: First-order approximation. *Journal of Geophysical Research*, *106*(A11), 26,017–26,032. https://doi.org/10.1029/2000JA900138

Kurth, W. S., Gurnett, D. A., Hospodarsky, G. B., Farrell, W. M., Roux, A., Dougherty, M. K., … Alexander, C. J. (2002). The dusk flank of Jupiter's magnetosphere. *Nature*, *415*(6875), 991–994. https://doi.org/10.1038/415991a

Ladreiter, H. P., & Leblanc, Y. (1989). Jovian hectometric radiation—Beaming, source extension, and solar wind control. *Astronomy and Astrophysics*, *226*, 297–310.

Luhmann, J. G., Walker, R. J., Russell, C. T., Crooker, N. U., Spreiter, J. R., & Stahara, S. S. (1984). Patterns of potential magnetic field merging sites on the dayside magnetopause. *Journal of Geophysical Research*, *89*(A3), 1739–1742. https://doi.org/10.1029/JA089iA03p01739

Ma, X., Delamere, P., Otto, A., & Burkholder, B. (2017). Plasma transport driven by the three-dimensional Kelvin-Helmholtz instability. *Journal of Geophysical Research: Atmospheres*, *122*. https://doi.org/10.1002/2017JA024394

Ma, X., Otto, A., & Delamere, P. A. (2014a). Interaction of magnetic reconnection and Kelvin-Helmholtz modes for large magnetic shear: 1. Kelvin-Helmholtz trigger. *Journal of Geophysical Research: Space Physics*, *119*, 781–797. https://doi.org/10.1002/2013JA019224

Ma, X., Otto, A., & Delamere, P. A. (2014b). Interaction of magnetic reconnection and Kelvin-Helmholtz modes for large magnetic shear: 2. Reconnection trigger. *Journal of Geophysical Research: Space Physics*, *119*, 808–820. https://doi.org/10.1002/2013JA019225

Ma, X., Stauffer, B., Delamere, P. A., & Otto, A. (2015). Asymmetric Kelvin-Helmholtz propagation at Saturn's dayside magnetopause. *Journal of Geophysical Research: Space Physics*, *120*, 1867–1875. https://doi.org/10.1002/2014JA020746

Masters, A. (2014). Magnetic reconnection at Uranus' magnetopause. *Journal of Geophysical Research: Space Physics*, *119*, 5520–5538. https://doi.org/10.1002/2014JA020077

Masters, A. (2015a). Magnetic reconnection at Neptune's magnetopause. *Journal of Geophysical Research: Space Physics*, *120*, 479–493. https://doi.org/10.1002/2014JA020744

Masters, A. (2015b). The dayside reconnection voltage applied to Saturn's magnetosphere. *Geophysical Research Letters*, *42*, 2577–2585. https://doi.org/10.1002/2015GL063361

Masters, A., Achilleos, N., Cutler, J. C., Coates, A. J., Dougherty, M. K., & Jones, G. H. (2012). Surface waves on Saturn's magnetopause. *Planetary and Space Science*, *65*(1), 109–121. https://doi.org/10.1016/j.pss.2012.02.007

McComas, D. J., & Bagenal, F. (2007). Jupiter: A fundamentally different magnetospheric interaction with the solar wind. *Geophysical Research Letters*, *34*, L20106. https://doi.org/10.1029/2007GL031078

McComas, D. J., Szalay, J. R., Allegrini, F., Bagenal, F., Connerney, J., Ebert, R. W., … Bolton, S. (2017). Plasma environment at the dawn flank of Jupiter's magnetosphere: Juno arrives at Jupiter. *Geophysical Research Letters*, *44*, 4432–4438. https://doi.org/10.1002/2017GL072831

Miura, A., & Pritchett, P. L. (1982). Nonlocal stability analysis of the MHD Kelvin-Helmholtz instability in a compressible plasma. *Journal of Geophysical Research*, *87*(A9), 7431–7444. https://doi.org/10.1029/JA087iA09p07431

Nakamura, T. K. M., Daughton, W., Karimabadi, H., & Eriksson, S. (2013). Three-dimensional dynamics of vortex-induced reconnection and comparison with THEMIS observations. *Journal of Geophysical Research: Space Physics*, *118*, 5742–5757. https://doi.org/10.1002/jgra.50547

Nichols, J. D., Badman, S. V., Bagenal, F., Bolton, S. J., Bonfond, B., Bunce, E. J., … Yoshikawa, I. (2017). Response of Jupiter's auroras to conditions in the interplanetary medium as measured by the Hubble Space Telescope and Juno. *Geophysical Research Letters*, *44*, 7643–7652. https://doi.org/10.1002/2017GL073029

Nichols, J. D., Bunce, E. J., Clarke, J. T., Cowley, S. W. H., Gérard, J.-C., Grodent, D., & Pryor, W. R. (2007). Response of Jupiter's UV auroras to interplanetary conditions as observed by the Hubble Space Telescope during the Cassini flyby campaign. *Journal of Geophysical Research*, *112*, A02203. https://doi.org/10.1029/2006JA012005

Nikutowski, B., Büchner, J., Otto, A., Kistler, L. M., Korth, A., Moukis, C., … Baumjohann, W. (2002). Equator-S observation of reconnection coupled to surface waves. *Advances in Space Research*, *29*, 1129–1134. https://doi.org/10.1016/S0273-1177(02)00030-3

Nykyri, K., Otto, A., Lavraud, B., Mouikis, C., Kistler, L. M., Balogh, A., & Rème, H. (2006). Cluster observations of reconnection due to the Kelvin-Helmholtz instability at the dawnside magnetospheric flank. *Annales Geophysicae*, *24*, 2619–2643. https://doi.org/10.5194/angeo-24-2619-2006

Ogilvie, K. W., & Fitzenreiter, R. J. (1989). The Kelvin-Helmholtz instability at the magnetopause and inner boundary layer surface. *Journal of Geophysical Research*, *94*(A11), 15,113–15,123. https://doi.org/10.1029/JA094iA11p15113

Paschmann, G., Øieroset, M., & Phan, T. (2013). In situ observations of reconnection in space. *Space Science Reviews*, *178*(2-4), 385–417. https://doi.org/10.1007/s11214-012-9957-2

Petrinec, S. M., Burch, J. L., Fuselier, S. A., Gomez, R. G., Lewis, W., Trattner, K. J., … Young, D. (2016). Comparison of Magnetospheric Multiscale ion jet signatures with predicted reconnection site locations at the magnetopause. *Geophysical Research Letters*, *43*, 5997–6004. https://doi.org/10.1002/2016GL069626

Petrinec, S. M., Fuselier, S. A., Funsten, H. O., Heirtzler, D., Janzen, P., Kucharek, H., … Wurz, P. (2011). Neutral atom imaging of the magnetospheric cusp. *Journal of Geophysical Research*, *116*, A07203. https://doi.org/10.1029/2010JA016357

Petrinec, S. M., Mukai, T., Nishida, A., Yamamoto, T., Nakamura, T. K., & Kokubun, S. (1997). Geotail observations of magnetosheath flow near the magnetopause, using wind as a solar wind monitor. *Journal of Geophysical Research*, *102*(A12), 26,943–26,959. https://doi.org/10.1029/97JA01637

Petrinec, S. M., & Russell, C. T. (1997). Hydrodynamic and MHD equations across the bow shock and along the surfaces of planetary obstacles. *Space Science Reviews*, *79*(3/4), 757–791. https://doi.org/10.1023/A:1004938724300

Petrinec, S. M., Trattner, K. J., & Fuselier, S. A. (2003). Steady reconnection during intervals of northward IMF: Implications for magnetosheath properties. *Journal of Geophysical Research*, *108*(A12), 1458. https://doi.org/10.1029/2003JA009979

Petrinec, S. M., Trattner, K. J., Fuselier, S. A., & Stovall, J. (2014). The steepness of the magnetic shear angle "saddle": A parameter for constraining the location of dayside magnetic reconnection? *Journal of Geophysical Research: Space Physics*, *119*, 8404–8414. https://doi.org/10.1002/2014JA020209

Phan, T.-D., Gosling, J. T., Paschmann, G., Pasma, C., Drake, J. F., Øieroset, M., … Davis, M. S. (2010). The dependence of magnetic reconnection on plasma β and magnetic shear: Evidence from solar wind observations. *Astrophysics Journal Letters*, *719*(2), L199–L203. https://doi.org/10.1088/2041-8205/719/2/L199

Phan, T.-D., Love, T. E., Gosling, J. T., Paschmann, G., Eastwood, J. P., Oieroset, M., … Auster, U. (2011). Triggering of magnetic reconnection in a magnetosheath current sheet due to compression against the magnetopause. *Geophysical Research Letters*, *38*, L17101. https://doi.org/10.1029/2011GL048586

Phan, T.-D., Paschmann, G., Gosling, J. T., Oieroset, M., Fujimoto, M., Drake, J. F., & Angelopoulos, V. (2013). The dependence of magnetic reconnection on plasma β and magnetic shear: Evidence from magnetopause observations. *Geophysical Research Letters*, *40*, 11–16. https://doi.org/10.1029/2012GL054528

Prangé, R., Chagnon, G., Kivelson, M. G., Livengood, T. A., & Kurth, W. (2001). Temporal monitoring of Jupiter's auroral activity with IUE during the Galileo mission. Implications for magnetospheric processes. *Planetary and Space Science*, *49*(3-4), 405–415. https://doi.org/10.1016/S0032-0633(00)00161-6

Prangé, R., Pallier, L., Hansen, K. C., Howard, R., Vourlidas, A., Courtin, R., & Parkinson, C. (2004). An interplanetary shock traced by planetary auroral storms from the Sun to Saturn. *Nature*, *432*(7013), 78–81. https://doi.org/10.1038/nature02986

Pryor, W. R., Stewart, A. I. F., Esposito, L. W., McClintock, W. E., Colwell, J. E., Jouchoux, A. J., … Dougherty, M. K. (2005). Cassini UVIS observations of Jupiter's auroral variability. *Icarus*, *178*(2), 312–326. https://doi.org/10.1016/j.icarus.2005.05.021

Richardson, J. D. (1987). Ion distributions in the dayside magnetosheaths of Jupiter and Saturn. *Journal of Geophysical Research*, *92*(A6), 6133–6140. https://doi.org/10.1029/JA092iA06p06133

Sanny, J., McPherron, R. L., Russell, C. T., Baker, D. N., Pulkkinen, T. I., & Nishida, A. (1994). Growth-phase thinning of the near-Earth current sheet during the CDSW 6 substorm. *Journal of Geophysical Research*, *99*(A4), 5805–5816. https://doi.org/10.1029/93JA03235

Slavin, J. A., & Holzer, R. E. (1979). The effect of erosion on the solar wind stand-off distance at Mercury. *Journal of Geophysical Research*, *84*(A5), 2076–2082. https://doi.org/10.1029/JA084iA05p02076

Slavin, J. A., & Holzer, R. E. (1981). Solar wind flow about the terrestrial planets 1. Modeling bow shock position and shape. *Journal of Geophysical Research*, *86*(A13), 11,401–11,418. https://doi.org/10.1029/JA086iA13p11401

Slavin, J. A., Imber, S. M., Boardsen, S. A., Di Braccio, G. A., Sundberg, T., Sarantos, M., … Solomon, S. C. (2012). MESSENGER observations of a flux-transfer-event shower at Mercury. *Journal of Geophysical Research*, *117*, A00M06. https://doi.org/10.1029/2012JA017926

Sonnerup, B. U. O. (1970). Magnetic field reconnection in a highly conducting incompressible fluid. *Journal of Plasma Physics*, *4*(01), 161–174. https://doi.org/10.1017/S0022377800004888

Southwood, D. J., & Kivelson, M. G. (2001). A new perspective concerning the influence of the solar wind on the Jovian magnetosphere. *Journal of Geophysical Research*, *106*(A4), 6123–6130. https://doi.org/10.1029/2000JA000236

Souza, V. M., Gonzalez, W. D., Sibeck, D. G., Koga, D., Walsh, B. M., & Mendes, O. (2017). Comparative study of three reconnection X line models at the Earth's dayside magnetopause using in situ observations. *Journal of Geophysical Research: Space Physics*, *122*, 4228–4250. https://doi.org/10.1002/2016JA023790

Swisdak, M., & Drake, J. F. (2007). Orientation of the reconnection X-line. *Geophysical Research Letters*, *34*, L11106. https://doi.org/10.1029/2007GL029815

Swisdak, M., Opher, M., Drake, J. F., & Bibi, F. A. (2010). The vector direction of the interstellar magnetic field outside the heliosphere. *The Astrophysical Journal*, *710*(2), 1769–1775. https://doi.org/10.1088/0004-637X/710/2/1769

Swisdak, M., Rogers, B. N., Drake, J. F., & Shay, M. A. (2003). Diamagnetic suppression of component magnetic reconnection at the magnetopause. *Journal of Geophysical Research*, *108*(A5), 1218. https://doi.org/10.1029/2002JA009726

Terasawa, T., Maezawa, K., & Machida, S. (1978). Solar wind effect on Jupiter's non-Io-related radio emission. *Nature*, *273*(5658), 131–132. https://doi.org/10.1038/273131a0

Trattner, K. J., Burch, J. L., Ergun, R., Fuselier, S. A., Gomez, R. G., Grimes, E. W., … Young, D. T. (2016). The response time of the magnetopause reconnection location to changes in the solar wind: MMS case study. *Geophysical Research Letters*, *43*, 4673–4682. https://doi.org/10.1002/2016GL068554

Trattner, K. J., Mulcock, J. S., Petrinec, S. M., & Fuselier, S. A. (2007a). Location of the reconnection line at the magnetopause during southward IMF conditions. *Geophysical Research Letters*, *34*, L03108. https://doi.org/10.1029/2006GL028397

Trattner, K. J., Mulcock, J. S., Petrinec, S. M., & Fuselier, S. A. (2007b). Probing the boundary between anti-parallel and component reconnection during southward interplanetary magnetic field conditions. *Journal of Geophysical Research*, *112*, A08210. https://doi.org/10.1029/2007JA012270

Trattner, K. J., Onsager, T. G., Petrinec, S. M., & Fuselier, S. A. (2015). Distinguishing between pulsed and continuous reconnection at the dayside magnetopause. *Journal of Geophysical Research: Space Physics*, *120*, 1684–1696. https://doi.org/10.1002/2014JA020713

Trattner, K. J., Petrinec, S. M., Fuselier, S. A., Omidi, N., & Sibeck, D. G. (2012). Evidence of multiple reconnection lines at the magnetopause from cusp observations. *Journal of Geophysical Research*, *117*, A01213. https://doi.org/10.1029/2011JA017080

Trattner, K. J., Thresher, S., Trenchi, L., Fuselier, S. A., Petrinec, S. M., Peterson, W. K., & Marcucci, M. F. (2017). On the occurrence of magnetic reconnection equatorward of the cusps at the Earth's magnetopause during northward IMF conditions. *Journal of Geophysical Research: Space Physics*, *122*, 605–617. https://doi.org/10.1002/2016JA023398

Trenchi, L., Marcucci, M. F., & Fear, R. C. (2015). The effect of diamagnetic drift on motion of the dayside magnetopause reconnection line. *Geophysical Research Letters*, *42*, 6129–6136. https://doi.org/10.1002/2015GL065213

Vasyliunas, V. M. (1975). Theoretical models of magnetic field line merging, 1. *Reviews of Geophysics and Space Physics*, *13*(1), 303–336. https://doi.org/10.1029/RG013i001p00303

Vines, S. K., Fuselier, S. A., Petrinec, S. M., Trattner, K. J., & Allen, R. C. (2017). Occurrence frequency and location of magnetic islands at the dayside magnetopause. *Journal of Geophysical Research: Space Physics*, *122*, 4138–4155. https://doi.org/10.1002/2016JA023524

Waite, J. H. Jr., Gladstone, G. R., Lewis, W. S., Goldstein, R., McComas, D. J., Riley, P., … Young, D. T. (2001). An auroral flare at Jupiter. *Nature*, *410*(6830), 787–789. https://doi.org/10.1038/35071018

Walker, R. J., Ogino, T., & Kivelson, M. G. (2001). Magnetohydrodynamic simulations of the effects of the solar wind on the Jovian magnetosphere. *Planetary and Space Science*, *49*(3-4), 237–245. https://doi.org/10.1016/S0032-0633(00)00145-8

Walker, R. J., & Russell, C. T. (1985). Flux transfer events at the Jovian magnetopause. *Journal of Geophysical Research*, *90*(A8), 7397–7404. https://doi.org/10.1029/JA090iA08p07397

Wang, S., Kistler, L. M., Mouikis, C. G., & Petrinec, S. M. (2015). Dependence of the dayside magnetopause reconnection rate on local conditions. *Journal of Geophysical Research: Space Physics*, *120*, 6386–6408. https://doi.org/10.1002/2015JA021524

Wilder, F. D., Eriksson, S., Trattner, K. J., Cassak, P. A., Fuselier, S. A., & Lybekk, B. (2014). Observation of a retreating X-line and magnetic islands poleward of the cusp during northward interplanetary magnetic field conditions. *Journal of Geophysical Research: Space Physics*, *119*, 9643–9657. https://doi.org/10.1002/2014JA020453

Zarka, P., & Genova, F. (1983). Low-frequency Jovian emission and solar wind magnetic sector structure. *Nature*, *306*(5945), 767–768. https://doi.org/10.1038/306767a0

Zwan, B. J., & Wolf, R. A. (1976). Depletion of solar wind plasma near a planetary boundary. *Journal of Geophysical Research*, *81*(10), 1636–1648. https://doi.org/10.1029/JA081i010p01636